Temperature Coefficients of Redox Potential of Solid Materials

Yuya Fukuzumi

September 2020

Temperature Coefficients of Redox Potential of Solid Materials

Yuya Fukuzumi

Doctoral Program in Physics

Submitted to the Graduate School of
Pure and Applied Sciences
in Partial Fulfillment of the Requirements
for the Degree of Doctor of Philosophy in
Science

at the
University of Tsukuba

Contents

Chapter 1

Introduction

1.1 Energy harvesting utilizing temperature coefficient of redox potential (α)

1.1.1 Needs of energy harvesting

Recently, energy harvesting technologies are intensively investigated and developed. One reason is the environmental problem. For effective use of energy resources, it is necessary to reduce the emission of extra heat from industry, transportation, and our daily life. In particular, the low-grade heat distributing between 30°C–60°C comprise the greater part of amount of the total emission from industry.[1–4] However, it is difficult to convert low-grade heat into another energy. Another reason is coming a new era of Internet of Things (IoT). To make IoT devices popular in our life, the devices have to get electricity from ambient energy sources[5] for example room light,[5,6] vibration on a floor,[5] and heat of air[5] or human body[5,7] because almost all of these devices are far from plug sockets. Thus, energy harvesting is one of the key technologies to realize the IoT society.

1.1.2 Tertiary battery

Tertiary battery is one of the promising devices for future energy harvesting. This device was proposed by Shibata *et al.*[8] in 2018, which converts thermal energy into electric power using temperature dependence of redox potential. The key parameter is the temperature coefficient ($\alpha \equiv \frac{\partial V}{\partial T}$) of redox potential ($V$). The tertiary battery consists of cathode, anode, and electrolyte. The cathode and the anode are made of different materials with different α [$\alpha_{\mathrm{cathode}}$ and α_{anode} ($< \alpha_{\mathrm{cathode}}$)]. The heating/cooling of the battery changes the cell voltage (V_{cell}) between anode and cathode. In other words, tertiary battery converts temperature itself into electric energy, making in a sharp contrast with the semiconductor-based thermoelectric devices. Figure 1.1 schematically shows a thermal cycle of the tertiary battery: (1) heating from the low temperature (T_{L}) to high temperature (T_{H}), (2) discharge at T_{H}, (3) cooling from T_{H} to T_{L}, and (4) discharge at T_{L}. Shibata *et al.*[8] demonstrated that tertiary battery whose cathode and anode were Prussian blue analogues {$\mathrm{Na}_x\mathrm{Co}[\mathrm{Fe}(\mathrm{CN})_6]_{0.71}$ (denoted as NCF71) and $\mathrm{Na}_x\mathrm{Co}[\mathrm{Fe}(\mathrm{CN})_6]_{0.90}$ (NCF90)} with different α produced electric energy with thermal efficiency (η) of 1% between T_{L} (= 295 K) and T_{H} (= 323 K).

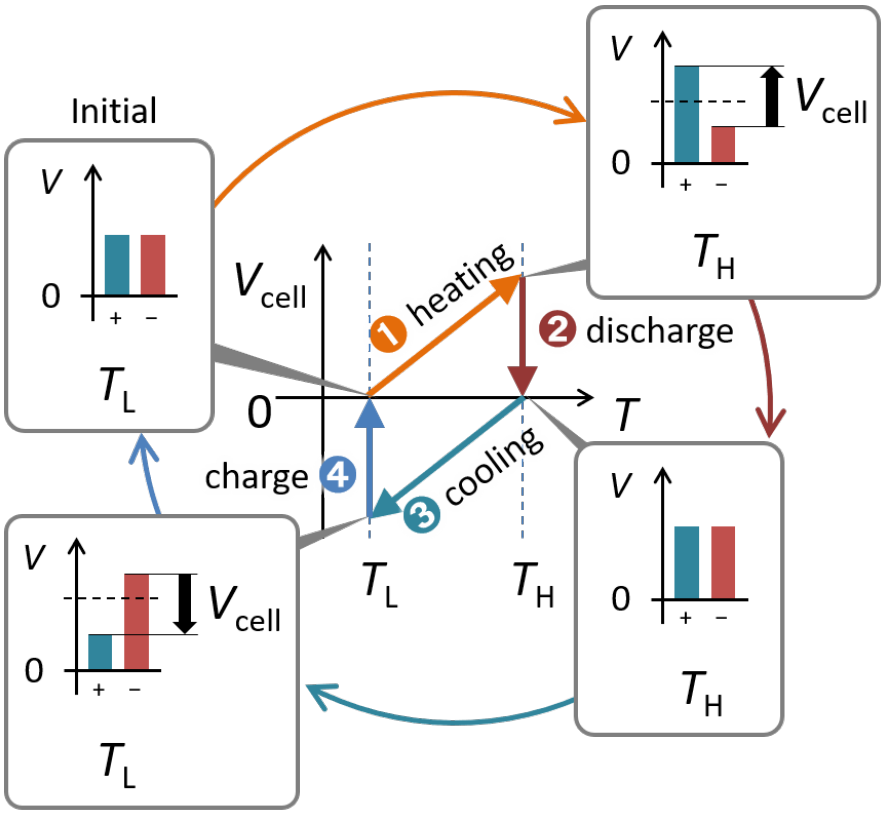

Figure 1.1: Schematic illustration of thermal cycle against cell voltage (V_{cell}) and temperature (T) of the thertiary battery. The cycle consists of four processes: (1) heating from the low temperature (T_{L}) to high temperature (T_{H}), (2) discharge at T_{H}, (3) cooling from T_{H} to T_{L}, and (4) discharge at T_{L}. The processes (1) and (3) are performed in the open circuit condition.

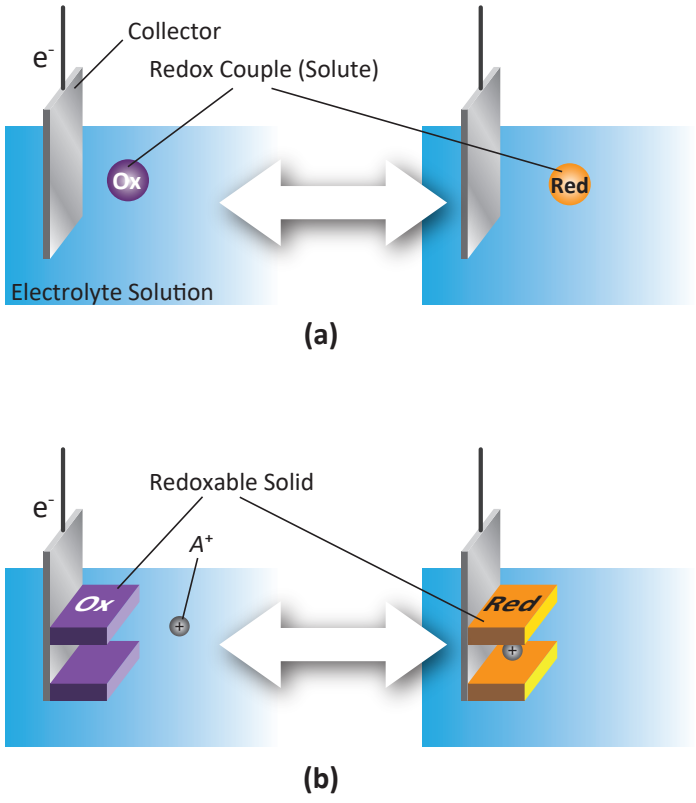

Figure 1.2: Schematic illustration of redox reactions of (a) solute and (b) solid.

1.1.3 Previous studies of α

There are many reports about temperature coefficient (α) of redox potential in various redox couples since long ago. For example, the most famous redox reaction is

$$[\mathrm{Fe(CN)_6}]^{3-} + \mathrm{e}^- \rightleftharpoons [\mathrm{Fe(CN)_6}]^{4-}. \tag{1.1}$$

Quickenden *et al.* reported that α of $[\mathrm{Fe(CN)_6}]^{3-}/[\mathrm{Fe(CN)_6}]^{4-}$ redox couple in an aqueous solution is equal to -1.5 mV/K,[9] which is known as one of high-α redox couples. In addition to the $[\mathrm{Fe(CN)_6}]^{3-}/[\mathrm{Fe(CN)_6}]^{4-}$ redox couple, many redox couples such as $\mathrm{Cu^+/Cu^{2+}}$, $\mathrm{Cd^+/Cd^{2+}}$ and, $\mathrm{LaCl_6}^{3-}/\mathrm{LaCl_4}^{2-}$ were investigated.[9] These redox couples are solutes dissolved in electrolyte solutions [Fig. 1.2 (a)].

There are few reports about α of solids [Fig. 1.2 (b)]. We note that the tertiary battery uses redoxable solid. To realize a tertiary battery with high-efficiency, it is important to explore high-α material. For this purpose, we first need to clarify the physical origin of α.

1.2 Physical origin of α

1.2.1 Interrelation between α and entropy

Let us suppose the following reduction reaction:

$$\mathrm{Ox} + A^+ + \mathrm{e}^- \longrightarrow \mathrm{Red}, \tag{1.2}$$

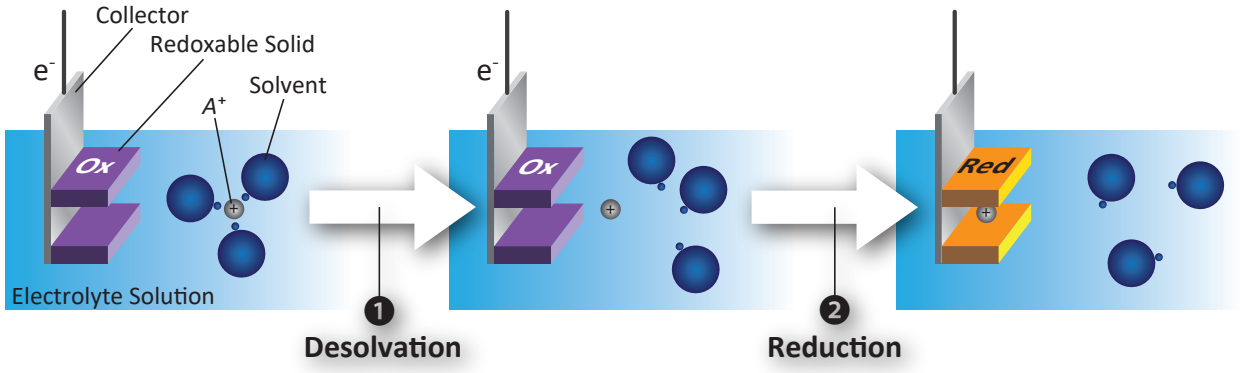

Figure 1.3: Schematic picture of reduction processes. In the (1) desolvation process, A^+ takes off the solvent molecules. In the (2) reduction process, A^+ is intercalated into the solid.

where Ox (Red), A^+, and e^- are chemical formula representing the oxidant (reductant), alkali metal ion, and electron, respectively. From a thermodynamical point of view, redox potential (V) is expressed with use of Gibbs free energy (G):

$$V = -\frac{1}{e}\Delta G, \tag{1.3}$$

where e is the elementary charge (> 0). ΔX represents difference in X between the reduced and oxidized states ($\Delta X \equiv X_{\mathrm{Red}} - X_{\mathrm{Ox}}$). The temperature coefficient (α) of V is given by:

$$\alpha \equiv \frac{\partial V}{\partial T} = -\frac{1}{e}\left(\frac{\partial \Delta G}{\partial T}\right)_p = \frac{1}{e}\Delta S, \tag{1.4}$$

where S is the entropy at constant pressure.

Magnitudes of S of solid materials can be evaluated by heat capacity measurement. For example, Loos *et al.*[10] reported S of $LiFePO_4$. S can be also evaluated by first principles calculations.[11,12] For example, Hinuma *et al.* evaluated S of alkali metals[13,14], $LiFePO_4/FePO_4$[13], and successive ordered state of $P2$-Na_xCoO_2 ($x = 1/2$, $2/3$, $10/13$, and $13/16$).[14] The calculated S of $LiFePO_4$are consistent with experimental data.[10]

1.2.2 Solid and electrolyte component of α

Figure 1.3 schematically shows the reduction reaction process. We note that the reduction reaction influence not only the solid system but also the electrolyte system, because A^+ is exchanged between solid and electrolyte. More specifically, the reaction consists of the following (1) desolvation process of A^+ and (2) reduction (intercalation) process of solid. We tentatively divided ΔS into the electrolyte ($\Delta S_{\mathrm{electrolyte}}$) and solid ($\Delta S_{\mathrm{solid}}$) components as follows:

$$\Delta S = \Delta S_{\mathrm{electrolyte}} + \Delta S_{\mathrm{solid}} \tag{1.5}$$

$$= \Delta S_{\mathrm{electrolyte}} + S_{\mathrm{Red}} - S_{\mathrm{Ox}}, \tag{1.6}$$

where S_{Red} (S_{Ox}) is entropy of the reductant (the oxidant). Thus, α is expressed as

$$\alpha = \alpha_{\mathrm{electrolyte}} + \alpha_{\mathrm{solid}} \tag{1.7}$$

$$= \alpha_{\mathrm{electrolyte}} + \frac{1}{e}\left(S_{\mathrm{Red}} - S_{\mathrm{Ox}}\right), \tag{1.8}$$

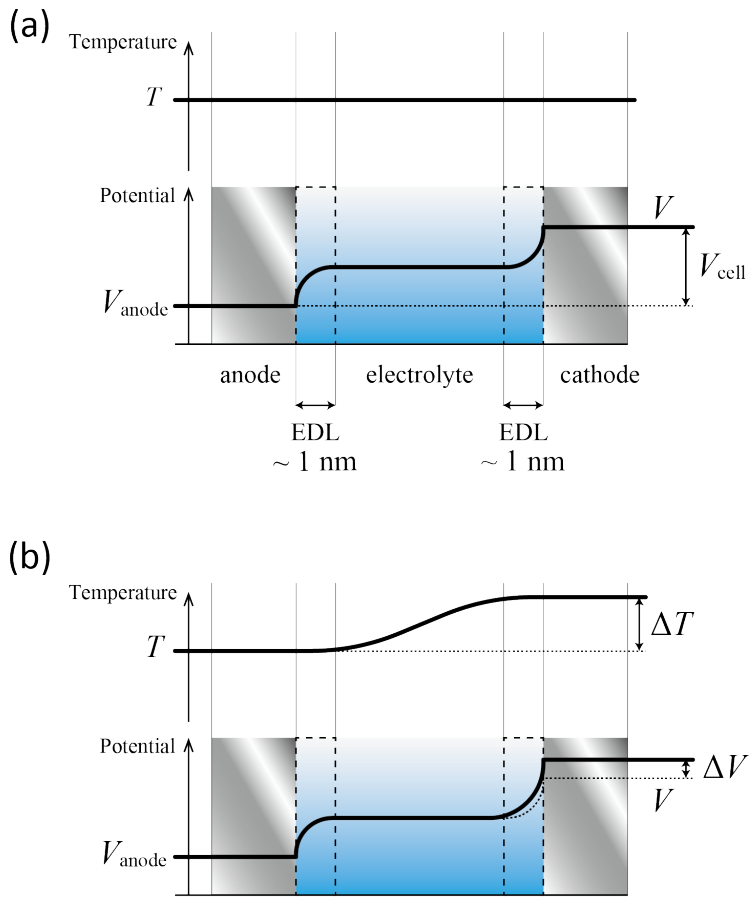

Figure 1.4: Schematic diagram of the potential (V) and temperature (T) variation in a battery, which consists of anode, electrolyte, and cathode. (a) without and (b) with temperature difference (ΔT). EDL means electric double layer. V and V_{anode} are the redox potentials of cathode and anode, respectively. V_{cell} is the cell voltage.

where $\alpha_{\mathrm{electrolyte}}$ $(= \frac{1}{e}\Delta S_{\mathrm{electrolyte}})$ and α_{solid} $(= \frac{1}{e}\Delta S_{\mathrm{solid}})$ are the electrolyte and solid component of α, respectively.

In solid system, S has several origins, such as vibrational entropy, configuration entropy of Li/Na, and configuration entropy of $3d$ electrons. Iwaizumi *et al.*[15] investigated α of several conjugated polymers. They concluded that vibrational entropy plays a significant role on α in conjugated polymers.

1.3 Redox potential and electric double layer

Here, let us explain the actual redox potential in a battery system, which consist of anode, cathode, and electrolyte. Figure 1.4 (a) schematically shows the potential along the anode-electrolyte-cathode direction. Even in the open circuit condition, voltage difference occurs due to a difference in redox potentials between the anode (V_{anode}) and cathode (V) materials. Therefore, ions in the electrolyte move to the electrode surface so as to cancel the potential gradient in the electrolyte. The layer consists of the moved ions is about $\sim$ 1 nm thick and is called an electric double layer (EDL). Importantly,

the redox reaction occurs at the electrode surface since the EDL localizes the potential change at the very vicinity (~ 1 nm) around the electrode surface. The voltage drop within EDL induces the redox reaction of each electrode. These are the actual image of the redox potential while the system reaches equilibrium. In the equilibrium condition (or zero current condition), the oxidation and reduction processes are balanced, and hence, there exists no net current. In other words, the redox potential is determined so that oxidation current and reduction current are the same.

What happens if we slightly change the cathode temperature to $T + \Delta T$ with fixing the anode temperature at T [Fig. 1.4 (b)]. The temperature gradience only exists in the electrolyte, because the thermal conductivities of electrodes are much higher than that of electrolyte. The temperature of the cathode EDL is essentially the same as the temperature of the cathode ($T + \Delta T$), since the thickness of the EDL is ~ 1 nm. The temperature change (ΔT) induces the potential change (ΔV). ΔT may slightly modify the ion distribution within the cathode EDL. The EDL effect, that is, slight modification of the ion distribution within the cathode EDL, on α is considered to be negligible because the potential change is still localized at the cathode surface. The potential change within the EDL balances the oxidization and reduction processes. In addition, as will be presented in the following chapters, we observed strong Li^+/Na^+ concentration (x) dependence of α in $Na_xM[Fe(CN)_6]_y$ (M = Fe, Mn, and Co) and $P2$-Na_xCoO_2. The x-dependence of α cannot be ascribed to the EDL effect, but to the cathode material effect. In this thesis, we will neglect the EDL effect. We focus our attention to the x-dependence of α in $Na_xM[Fe(CN)_6]_y$, $P2$-Na_xCoO_2, and Li_xFePO_4.

1.4 Purpose of this thesis

The purposes of this thesis are (1) precise determination of α to prototypical redoxable materials and (2) discussion on the microscopic origin of S ($\equiv e \times \alpha$). For the latter purpose, we experimentally subtracted the electrolyte component ($\Delta S_{\mathrm{electrolyte}}$). Unfortunately, experimental determination of $\Delta S_{\mathrm{electrolyte}}$ is quite difficult. So, we indirectly evaluated $\Delta S_{\mathrm{electrolyte}}$ with use of the relation:

$$\Delta S_{\mathrm{elecctrolyte}} = e\alpha - \Delta S_{\mathrm{solid}}. \tag{1.9}$$

We selected a most prototypical metal, that is, alkali metal ($A = \mathrm{Li}, \mathrm{Na}$), and experimentally determine α. $\Delta S_{\mathrm{solid}}$ is the same as S_A, because its reduction process is simple precipitation of one Li/Na on the metal surface.

We choose three materials, that is, Li_xFePO_4, $P2$-Na_xCoO_2, and Prussian blue analogues (PBAs). Li_xFePO_4 is a prototypical cathode material for Li-ion secondary battery. In the charge/discharge process, Li_xFePO_4 shows ideal phase separation into $FePO_4$ and $LiFePO_4$, as $Li_xFePO_4 \longrightarrow (1-x)FePO_4$ and $xFePO_4$. This means that addition of one Li^+ means increase of $LiFePO_4$ and decrease of $FePO_4$. Then, $\Delta S_{\mathrm{solid}}$ is the same as $S_{\mathrm{LiFePO_4}} - S_{\mathrm{FePO_4}}$, where $S_{\mathrm{LiFePO_4}}$ and $S_{\mathrm{FePO_4}}$ are the entropy of $LiFePO_4$ and $FePO_4$, respectively. $P2$-Na_xCoO_2 is a prototypical cathode material for Na-ion secondary battery. In the charge/discharge process, $P2$-Na_xCoO_2 shows successive phase transition at specific Na concentration (x_i; $i = 1, 2, 3, ...$) accompanying ordering of Na^+ ions. By means of a first principles calculation, Hinuma *et al.* have investigated the ordering structure of $P2$-Na_xCoO_2.[16] Therefore, phase separation is expected at the intermediation Na concentration (x; $x_i < x < x_{i+1}$). PBAs are promising cathode materials for Li- and Na-ion secondary battery. PBAs do not show

phase separation, except for $Li_xCo[Fe(CN)_6]_{0.90}$.[17] Then, we should consider the effect on variation of entropy, when one Na^+ and one electron are added.

The clue for the origin of ΔS_{solid} are (1) Li/Na concentration (x) dependence of α (Li_xFePO_4 and $P2$-Na_xCoO_2) or (2) redox site dependence of α (PBA). In the latter case, we investigated three kinds of PBAs, that is, $Na_xCo[Fe(CN)_6]_{0.71}$ (denoted as NCF71), $Na_xCo[Fe(CN)_6]_{0.90}$ (NCF90), and $Na_xMn[Fe(CN)_6]_{0.83}$ (NCF83). We observed characteristic redox site dependence of α and will interpret the dependence in terms of (1) $3d$-electron configuration entropy and (2) vibrational entropy of the CN^- related mode.

1.5 Contents of this thesis

Chapter 1 (this chapter) is devoted for background, the motivation, and purpose of this thesis. Chapter 2 describes experimental method, including sample preparation, characterization, and a specially-designed thermocell for α determination. Chapter 3 is devoted for results and discussion on α of alkali metals in several kinds of electrolyte. We evaluate electrolyte components ($\alpha_{electrolyte}$) of α with use of calculated entropies. Chapter 4 is devoted for results and discussion on α of Li_xFePO_4 against x. We compare the immaterial results with the entropy obtained by first principles calculation.[13] Chapter 5 is devoted for results and discussion on α of $P2$-Na_xCoO_2 against x. We observed serious discrepancy between the experimental data and first principles calculation. We interpret the discrepancy in terms of the residual configuration entropy of Na^+. Chapter 6 is devoted for results and discussion on α of PBAs against x. We discuss the redox site dependence of α in terms of $3d$-electron configuration entropy and vibriational entropy of the CN^- related mode.

Chapter 2

Experiments

2.1 Sample preparation

2.1.1 Li_xFePO_4

Preparation of electrode

Commercially available $LiFePO_4$ electrode (Hosen Co. Ltd., $LiFePO_4$: acetyleneblack : PVDF = 90 : 5 : 5 in weight) was used.

Synchrotron X-ray diffraction

Synchrotron radiation X-ray powder diffraction (XRD) measurements were performed at the BL02B2 beamline[18] at SPring-8. The fully-charged/-discharged active electrode was removed from the Al collector and was filled in a 300 μm quartz capillary. For the charge/discharge method, see Section 2.2. The capillary was placed at the Debye Scherrer camera. The wavelength of the X-rays (= 0.69963 Å) was calibrated using the lattice parameter of standard CeO_2 powder. The XRD patterns were monitored with an one-dimensional semiconductor detector (MYTHEN, Dectries Ltd.). The exposure time was 5 min.

In both the patterns of the fully-charged and -discharged Li_xFePO_4, all the reflections can be assigned by single-phase orthorhombic structure ($Pnma$; $Z = 4$), as shown in Fig. 2.1. The structural parameters were refined using the Rietan-FP program,[19] and are listed in Table 2.1 and Table 2.2. The lattice constants, *i.e.*, a, b, and c, are essentially the same as those of $LiFePO_4$ and $FePO_4$.[20] Hereafter, we regard the charged and discharged states as $x = 0$ and 1, respectively.

2.1.2 $P2$-Na_xCoO_2

Preparation of electrode

Polycrystalline sample of $P2$-$Na_{0.7}CoO_2$ was prepared by solid state reaction. Na_2CO_3 and Co_3O_4 were mixed in a 105 : 100 atomic ratio and calcined at 800°C in air for 40 hours. To avoid hydration, the compound was kept in vacuum immediately after the calcination. To obtain the $P2$-$Na_{0.7}CoO_2$ electrode, a mixture of sample powder, ketchen black (KB), and polyvinylidene difluoride (PVDF) in 8 : 1 : 1 weight ratio was pasted on an Al foil.

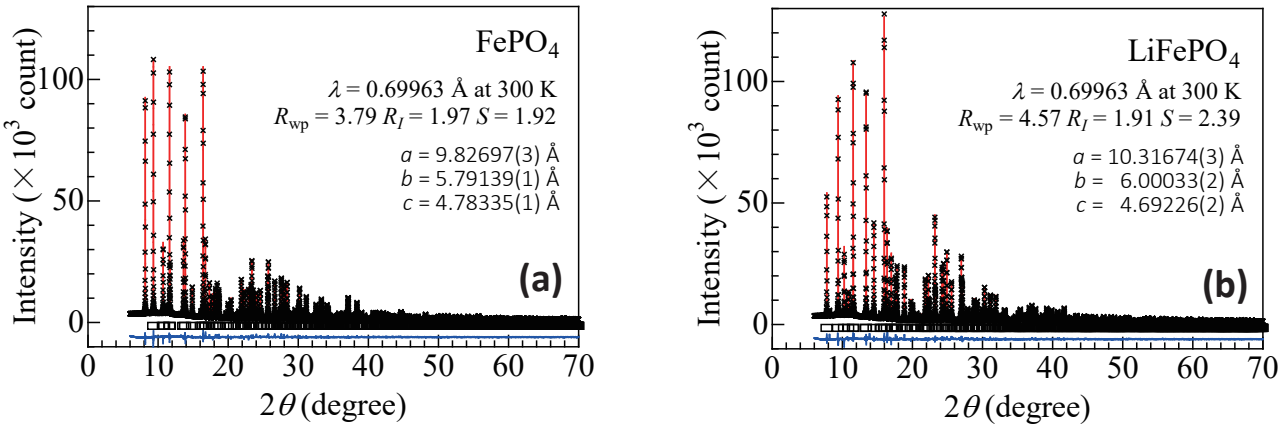

Figure 2.1: Rietveld refinements of X-ray powder diffraction patterns of Li_xFePO_4 in (a) the fully-charged electrode and (b) the fully-discharged electrode at 300 K. Crosses and the solid curves are experimental data and Rietveld refinements, respectively. Lower curves are the differences between experiment and calculation. The data were cited and modified from Ref [13].

Table 2.1: Occupancy (g), atomic coordinates (x, y, z), and atomic displacement parameter (B) of $LiFePO_4$ in the fully-discharged electrode as refined by the Rietveld method ($Pnma$; $Z = 4$). $a = 9.82697(3)$ Å, $b = 5.79139(1)$ Å, and $c = 4.78355(1)$ Å. R_{wp}, R_I, and S are 4.57, 1.91, and 2.39, respectively. The data were cited from Ref. [13].

atom	cite	g	x	y	z	B (Å^2)
Li	4a	1	0	0	0	2.17(13)
Fe	4c	1	0.21778(3)	1/4	0.52551(8)	0.39(1)
P	4c	1	0.40510(7)	1/4	0.8256(14)	0.25(1)
O1	4c	1	0.40222(17)	1/4	0.75728(32)	0.35(2)
O2	4c	1	0.04445(18)	1/4	0.29687(32)	0.35
O3	8d	1	0.33314(12)	0.04474(18)	0.21700(20)	0.45

Table 2.2: Occupancy (g), atomic coordinates (x, y, z), and atomic displacement parameter (B) of $FePO_4$ in the fully-charged electrode as refined by the Rietveld method ($Pnma$; $Z = 4$). $a = 10.31674(3)$ Å, $b = 6.00033(2)$ Å, and $c = 4.69226(2)$ Å. R_{wp}, R_I, and S are 3.79, 1.917 and 1.92, respectively. The data were cited from Ref. [13].

atom	cite	g	x	y	z	B (Å^2)
Fe	4c	1	0.22547(8)	1/4	0.54783(6)	0.28(1)
P	4c	1	0.40669(6)	1/4	0.89981(12)	0.15(1)
O1	4c	1	0.38106(12)	1/4	0.78692(25)	0.15(1)
O2	4c	1	0.05813(13)	1/4	0.33772(14)	0.15
O3	8d	1	0.33198(9)	0.04370(15)	0.24930(17)	0.15

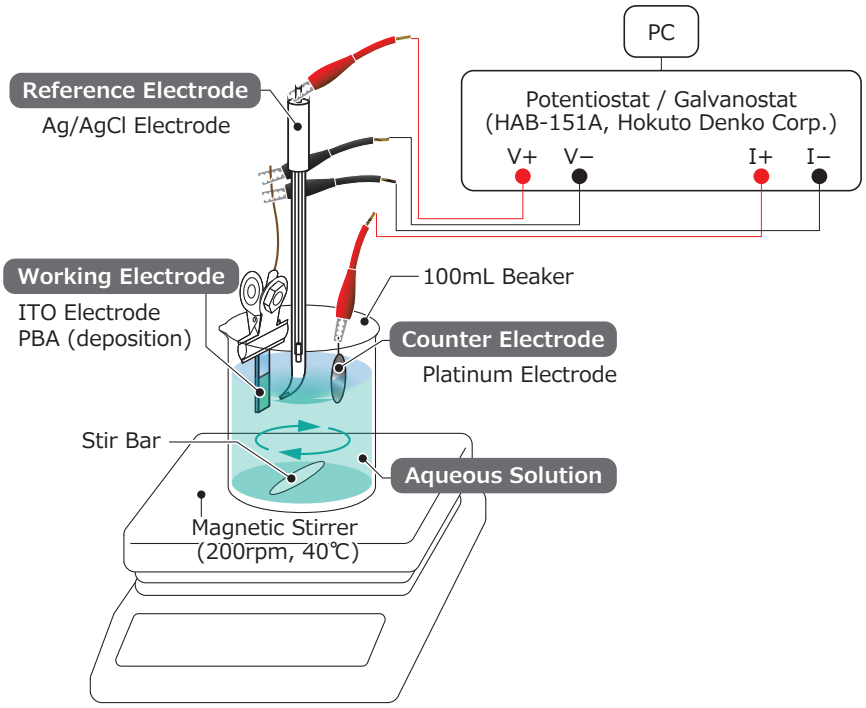

Figure 2.2: Schematic illustration of the electrochemical deposition system.

2.1.3 Prussian blue analogues

Preparation of electrode

Thin films of $Na_xCo[Fe(CN)_6]_{0.71}$ (NCF71), $Na_xCo[Fe(CN)_6]_{0.90}$ (NCF90), and $Na_xMn[Fe(CN)_6]_{0.83}$ (NCF83) were synthesized by electrochemical deposition on an indium tin oxide (ITO) transparent electrode. Figure 2.2 shows the schematic illustration of the electrochemical deposition system. The system consists of an ITO electrode as the working electrode, an Ag/AgCl electrode as the reference electrode, a Pt electrode as the counter electrode, and aqueous solution. The aqueous solutions used for the respective films (NCF71, NCF90, NMF83) are listed in Table 2.3. Before the deposition, the surface of the ITO electrode was purified by electrolysis of water adding 0.1 mol/L nitric acid for several minutes. In the deposition process, sawtooth modulation between −0.8 V and −0.1 V at 71 Hz was added, which enhances the ⟨111⟩ orientation. During the deposition, the aqueous solution was stirred at 200 rpm with a stir bar. The deposition times for respective films are listed in Table 2.3. Details of the synthesis conditions are described in literature.[21–23] The chemical composition of the film was determined by the inductively coupled plasma (ICP) method and CHN organic elementary analysis. The film thickness was about 1 μm, which was determined by a profilometer (BRUKER Dektak3030).

2.2 Electrochemical measurement

The electrochemical properties of the electrodes were investigated with a potentiostat (HokutoDENKO, HJ1001SD8) in beaker-type two-pole cells (Fig. 2.3). The combinations of cathode, anode, and elec-

Table 2.3: List of the electrochemical deposition conditions

Chemical composition	Aqueous solution	Deposition time
$Na_{0.84}Co[Fe(CN)_6]_{0.71}\cdot 3.8\,H_2O$ (NCF71)	0.5 mmol/L $K_3[Fe(CN)_6]$ 1.25 mmol/L $Co(NO_3)_2\cdot 6.0\,H_2O$ 1.0 mol/L $NaNO_3$	15 min
$Na_{1.60}Co[Fe(CN)_6]_{0.90}\cdot 2.9\,H_2O$ (NCF90)	0.8 mmol/L $K_3[Fe(CN)_6]$ 0.5 mmol/L $Co(NO_3)_2\cdot 6.0\,H_2O$ 5.0 mol/L $NaNO_3$	30 min
$Na_{1.24}Mn[Fe(CN)_6]_{0.83}\cdot 3.0\,H_2O$ (NMF83)	1.0 mmol/L $K_3[Fe(CN)_6]$ 1.5 mmol/L $MnCl_2\cdot 3.5\,H_2O$ 1.0 mol/L NaCl	15 min

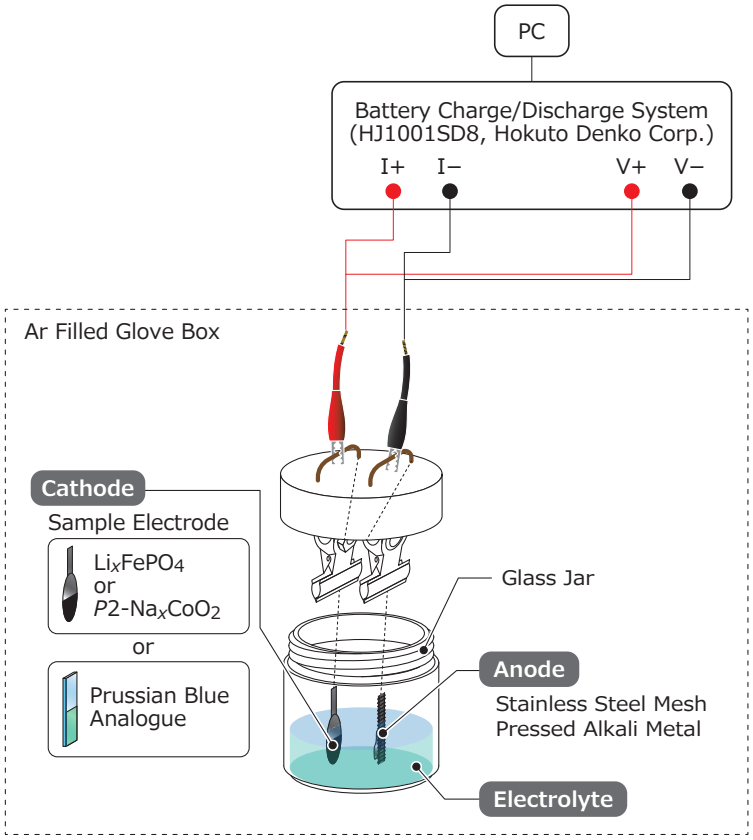

Figure 2.3: Schematic illustration of the beaker-type two-pole cell.

Table 2.4: Parameters of the electrochemical measurement. EC/DEC and PC represent ethylene carbonate / diethyl carbonate (1:1 volume) and propylene carbonate, respectively.

Cathode	Solvent	Solute	Anode	Charge/ discharge rate	Cut-off voltage (V)
Li_xFePO_4	EC/DEC	1 M $LiClO_4$	Li	0.1 C	3.0–4.0
$P2$-Na_xCoO_2	PC	1 M $NaClO_4$	Na	0.1 C	2.0–3.5
NCF71	PC	1 M $NaClO_4$	Na	1 C	2.0–4.0
NCF90	PC	1 M $NaClO_4$	Na	1 C	2.0–3.9
NMF83	PC	1 M $NaClO_4$	Na	1 C	2.0–4.2

trolyte are listed in Table 2.4. The active areas of the electrodes were *ca.* 0.5 cm^2 in Li_xFePO_4 and $P2$-Na_xCoO_2 and *ca.* 1 cm^2 in PBA. The mass of Li_xFePO_4 and $P2$-Na_xCoO_2 was evaluated using a electronic balance. The mass of each PBA was evaluated from thickness, area, and ideal density. The charge/discharge rates and the cut-off voltages are also listed in Table 2.4. The charge/discharge measurements were performed under Ar atmosphere in an Ar filled glove box.

2.3 Measurement of α

2.3.1 Electrolyte components

The magnitudes of α were carefully determined with use of specially-designed thermocell (Fig. 2.4). The electrolyte was filled in a ϕ7.3 mm polytetrafluoroethylene (PTFE) tube. The both ends are sealed with the Al pedestals, on which anode and cathode materials are attached. The two electrodes were placed strictly parallel with a distance of 2 mm, which causes pseudo one-dimensional thermal gradient within the electrolyte solution. The temperatures of cathode (T) and anode ($T_{\rm anode}$) were monitored with T-type thermocouples. The thermocouples are attached at the pedestals at a distance of 2 mm from the electrode-electrolyte interfaces. T and $T_{\rm anode}$ were independently controlled with Peltier modules attached at the bottom of the pedestals. The redox potential (V) of the cathode was carefully measured against T with fixing $T_{\rm anode}$ at ambient temperature. We note that the Seebeck coefficient ($\sim -2\mu$V/K) of the Al pedestal is negligible as compared with the observed α (≤ 0.7 mV/K). The magnitude of the temperature difference ($|T - T_{\rm anode}|$) between the electrodes was less than 10 K.

For the measurement of alkali metal (A), small piece of the same A were attached on the Al foil. The foils were attached on the Al pedestals. For the measurement of Li_xFePO_4, $P2$-Na_xCoO_2, and PBAs, alkali metal was used as anode. The combinations of the cathode, the anode, and electrolyte were the same as those in the electrochemical measurements (Table 2.4). The active area of the cathode in the thermocell was about 0.28 cm^2. The cell voltage ($V_{\rm cell}$) was carefully measured against T under the open circuit condition. The x value was controlled by discharge process with the discharge rate listed in Table 2.4. To establish the thermal equilibrium state of the cathode material, the measurement at each x was carried out at interval of two hours or more.

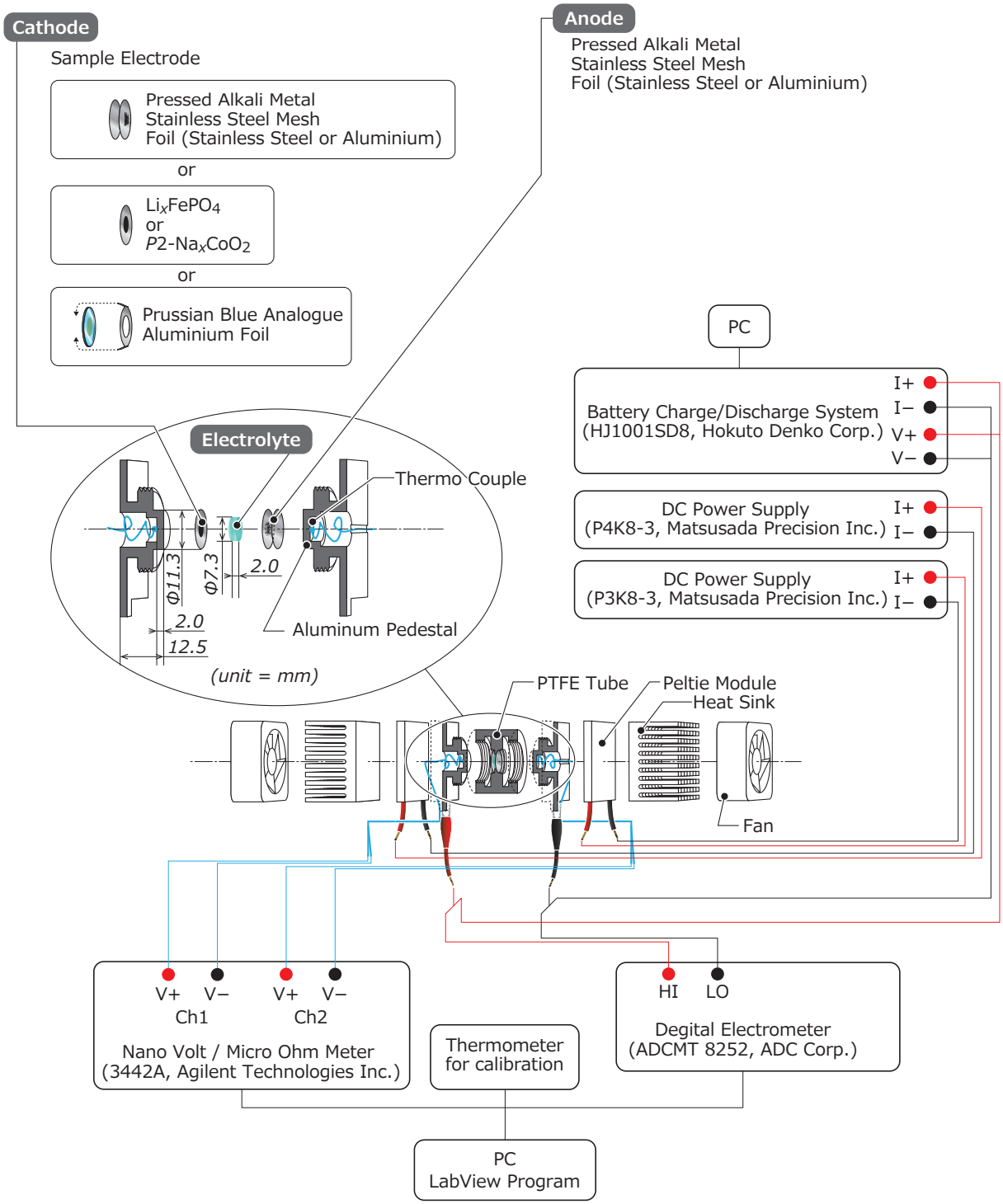

Figure 2.4: Illustration of specially-designed thermocell. Scales are in mm units.

Chapter 3

Electrolyte components of α

3.1 Results

Figure 3.1(a) shows temperature dependence of redox potential (V) of Li with two kinds of electrolyte solutions, *i.e.*, EC/DEC and GBL. In both the cases, V linearly increases with T. The α values were evaluated by least-squares fittings, as indicated by solid straight lines. In Table 3.1, α of Li against electrolyte solutions are summarized. α of Li slightly depends on the electrolyte solutions; α is 0.76 and 0.88 mV/K in EC/DEC and GBL, respectively.

Figure 3.1(b) shows temperature dependence of redox potential (V) of Na with four kinds of electrolyte solutions, *i.e.*, EC/DEC, GBL, PC, and DME. In EC/DEC, GB, and PC, α of Na scarcely depends on the electrolyte solutions; α is 0.77, 0.73, and 0.71 mV/K in EC/DEC, GBL, and PC, respectively. In Table 3.1, α of Na against electrolyte solutions are summarized. We emphasize that α (= 1.70 mV/K) of Na in DME is significantly larger than those in other solutions. Thus, the magnitude of the solvent effect shows significant solvent dependence. We note that DME has no carbonyl group in sharp contrast with the other solvents. This implies that the observed solvent dependence is ascribed to existence/absence of carbonyl group.

Let us evaluate the electrolyte component ($\alpha_{\rm electrolyte} = \alpha - \alpha_{\rm solid}$) of α. Hinuma *et al.*[14] calculated entropy (S_A) of Li and Na by first principles calculation: S_A of Li and Na at 300 K are 0.29 meV and

Table 3.1: α and its electrolyte component ($\alpha_{\rm electrolyte}$) against alkali metal (A) in several kinds of electrolyte. EC, DEC, GBL, PC, and DME represent ethylene carbonate, diethyl carbonate, γ-buthyro-lactone, propylene carbonate, and 1,2-dimethoxyethane, respectively. $\frac{1}{e}S_A$ is cited from Ref. [14]

A	Solute	Solvent	α (mV/K)	$\frac{1}{e}S_A$ (mV/K)	$\alpha_{\rm electrolyte}$ (mV/K)
Li	1M $LiClO_4$	EC/DEC	0.76	0.29	0.47
Li	1M $LiClO_4$	GBL	0.88	0.29	0.59
Na	1M $NaClO_4$	EC/DEC	0.77	0.52	0.25
Na	1M $NaClO_4$	GBL	0.73	0.52	0.21
Na	1M $NaClO_4$	PC	0.71	0.52	0.19
Na	1M $NaClO_4$	DME	1.70	0.52	1.18

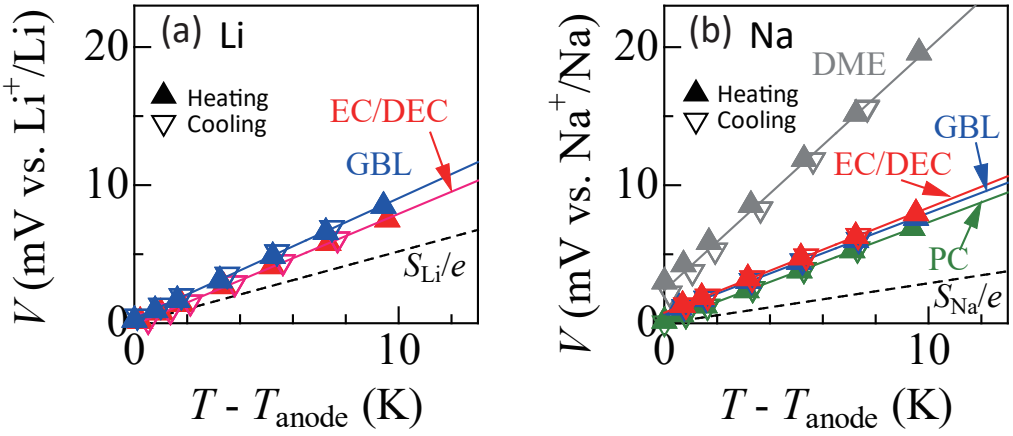

Figure 3.1: Temperature dependence of V of (a) Li and (b) Na. EC, DEC, GBL, PC, and DME represent ethylene carbonate, diethyl carbonate, γ-buthyro-lactone, propylene carbonate, and 1,2-dimethoxyethane, respectively. Open and closed symbols represent that the data are obtained in the heating and cooling runs, respectively. Solid straight lines are results of least-squares fittings. Broken straight lines show $\frac{1}{e}S_A$ of solid A cited from Ref. [14] For comparison of the slopes of the data, temperatures of anode ($T_{\rm anode}$) are subtracted from the respective temperatures of cathode (T). In (a) Li, $T_{\rm anode}$ was fixed at 289 K and 297 K for EC/DEC and GBL, respectively. In (b) Na, $T_{\rm anode}$ was fixed at 299 K, 301 K, 295 K, and 295 K for EC/DEC, GBL, PC, and DME, respectively. Error bars (≤ 0.01 mV) are within the symbol size. The data were cited and modified from Ref. [24].

0.52 meV, respectively. The broken straight line in Fig. 3.1 (a) represents the calculated $\frac{1}{e}S_A$. The slopes of the experimental data are much steeper than the calculated $\frac{1}{e}S_A$. A similar trend is also observed for Na [Fig. 3.1 (b)]. These indicate that the solvent effect on α is important and can never be neglected. Here after, we call $\frac{1}{e}S_A$ and $\alpha - \frac{1}{e}S_A$ as the solid ($\alpha_{\rm solid}$) and the electrolyte components ($\alpha_{\rm electrolyte}$), respectively. $\alpha_{\rm solid}$ and $\alpha_{\rm electrolyte}$ are also listed in Table 3.1.

3.2 Discussion

Here, let us discuss the microscopic origin of the solvent effect on α, *i.e.*, the variation of $\Delta S_{\rm electrolyte}$ of the solution when one A^+ is dissolved. If one A^+ is dissolved in solvent, the surrounding solvent molecules are forcedly aligned with negatively polarized moieties towards A^+. Such an alignment of the solvent molecules, or solvation effect, decreases configuration entropy. This argument is consistent with the experimental observation: $\alpha_{\rm electrolyte}$ (Table 3.1) is positive. In addition, in the case of EC/DEC and GBL, the solvent contribution is larger for Li^+ as compared with that for Na^+. This is reasonable because the solvation effect is stronger in the smaller Li^+.

Finally, let us briefly comment on the above-discussed solvent effect on the actual tertiary battery. In the tertiary battery,[8] the cathode and anode are in contact with the same electrolyte solution and at the same temperature ($T_{\rm anode} = T$). In this case, the solvent effect at cathode completely cancel that at anode, because one A^+ is dissolved in solvent when one A precipitates at another electrode. In other words, $\frac{\partial V_{\rm cell}}{\partial T}$ ($= \alpha_{\rm cathode} - \alpha_{\rm anode}$; where $\alpha_{\rm catnode}$ and $\alpha_{\rm anode}$ are the temperature coefficients

of redox potential at cathode and anode, respectively) is free from the solvent effect.

Chapter 4

Li_xFePO_4

4.1 Introduction

Li_xFePO_4 is one of the most prototypical intercalation compounds used as a cathode for lithium-ion secondary batteries. Li_xFePO_4 shows an average voltage of 3.5 V vs. Li^+/Li and a high capacity of $\geq$ 100 mAh/g.[25] The average voltage, however, is slightly low as compared with those of Li_xCoO_2, Li_xNiO_2, and $Li_xMn_2O_4$. Li_xFePO_4 forms a three-dimensional porous framework[25] consisting of FeO_6 octahedra and PO_4 tetrahedra, in which PO_4 tetrahedron share two corners with neighboring two FeO_6 octahedra and one edge with another octahedron (see Fig. 4.1). The nanopores of the framework can reversibly accommodate Li^+. The Li^+ deintercalation oxidizes Fe^{2+} to Fe^{3+} and significantly reduces the Fe–O bond length. Such a bond contraction is responsible for the phase separation (PS) into $LiFePO_4$ and $FePO_4$.[20,26–29] On the basis of the macroscopic nature of the PS, Delmas *et al.*[20] proposed that the Li^+ deintercalation and subsequent phase transformation into $FePO_4$ takes place at the $LiFePO_4$–$FePO_4$ boundary and not in the $LiFePO_4$ matrix. In this picture, the redox potential is essentially independent of Li concentration (x) because the deintercalation process of Li_xFePO_4 is expressed as $LiFePO_4 \longrightarrow FePO_4 + Li^+ + e^-$.

4.2 Results

Figure 4.2 shows the discharge curve of Li_xFePO_4. V is found to be the constant ($\sim$ 3.3 V) except in the high-x region ($x > 0.9$) near the end of the discharge curve. The obtained curve is essentially the same as the discharge curve reported in the letrature.[25]

Figure 4.3 shows temperature dependence of V of Li_xFePO_4 for $x = 0.2$ and 0.8. Closed and open symbols represent the data obtained in the heating and cooling runs, respectively. The data in the cooling run well trace those in the heating run, indicating that there is no thermal hysteresis nor degradation of the active material. At $x = 0.2$, V linearly increases with T. α (= 0.91 mV/K) was evaluated by least-squares fitting, as indicated by solid straight line. Similarly, V linearly increases with T at a rate of 0.91 mV/K at $x = 0.8$. Figure 4.4 shows the determined α of Li_xFePO_4 against x. α ($\sim$ 0.91 mV/K) is almost independent of x except in the high-x region ($\geq$ 0.9) near the edge of the discharge curve.

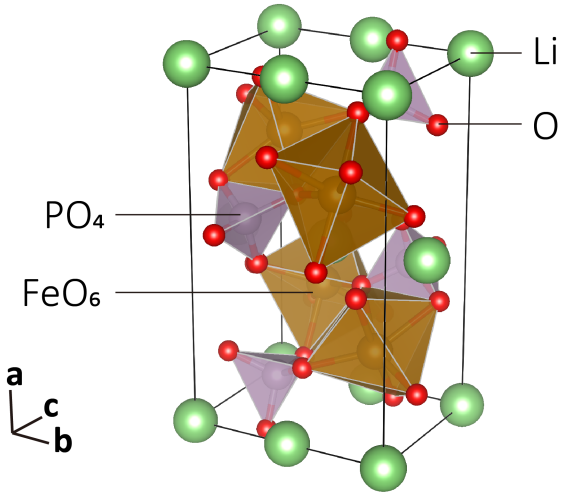

Figure 4.1: Crystal structure of Li_xFePO_4. Octahedra, tetrahedra, and large spheres represent FeO_6, PO_4, and Li site, respectively

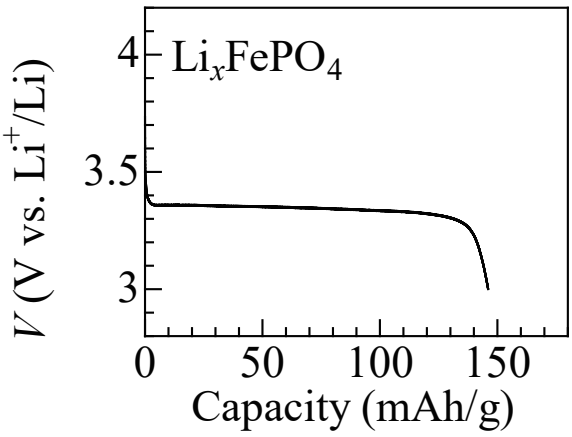

Figure 4.2: Discharge curve of Li_xFePO_4. The discharge rate was 0.1 C.

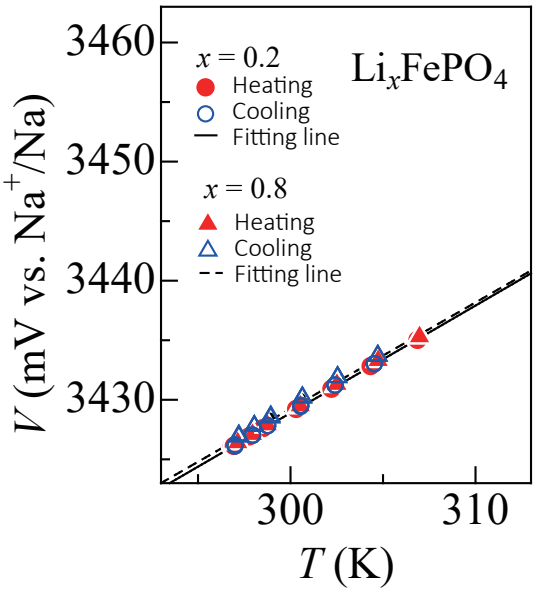

Figure 4.3: Temperature dependence of V of Li_xFePO_4 at $x = 0.2$ and 0.8 with T_{anode} fixed at 297 K. Solid straight lines are results of least-squares fittings in the heating run. Red closed and blue open symbols represent the data obtained in the heating and cooling runs, respectively. The data were cited and modified from Ref. [13)]

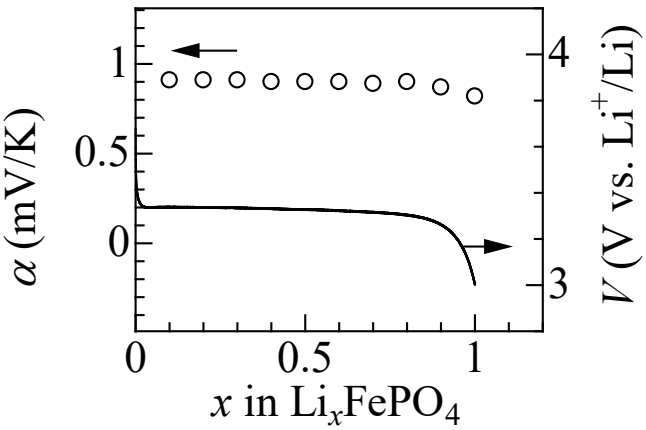

Figure 4.4: Temperature coefficient (α) of redox potential of Li_xFePO_4. The average values in the heating and cooling runs were plotted. The difference (≤ 0.02 mV/K) of α between the heating and cooling runs is within the symbol size. The black curve represents a discharge curve of Li_xFePO_4 at 0.1 C. The data were cited and modified from Ref. [13)]

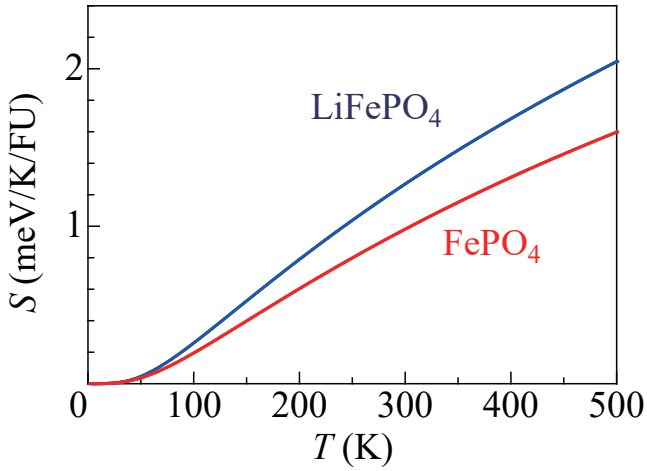

Figure 4.5: Calculated entropy (S) of $LiFePO_4$ and $FePO_4$ per formula unit against temperature. The data were cited and modified from Ref. [13)]

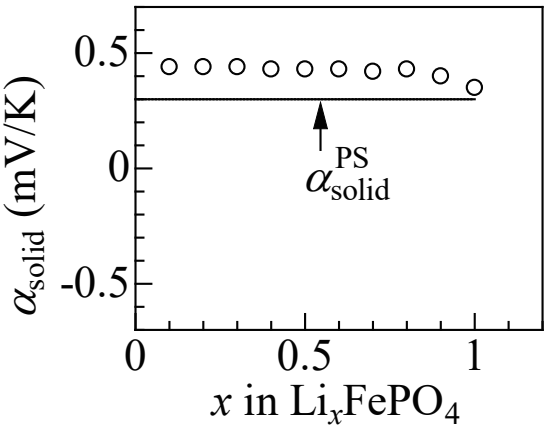

Figure 4.6: Solid component ($\alpha_{\mathrm{solid}} = \alpha - \alpha_{\mathrm{electrolyte}}$) of α of Li_xFePO_4. The solid line represents calculated $\alpha^{\mathrm{PS}}_{\mathrm{solid}}$.

4.3 Discussion

In Chapter 3, the electrolyte component ($\alpha_{\mathrm{electrolyte}}$) of α in EC/DEC containing 1 mol/L $LiClO_4$ was evaluated ($\alpha_{\mathrm{electrolyte}} = 0.47$ mV/K). On the other hand, α of Li_xFePO_4 is 0.91 mV/K irrespective of x. Then, the residual amount (= 0.44 mV/K) is ascribed to the solid component (α_{solid}) due to the chemical change from $FePO_4$ to $LiFePO_4$. Figure 4.6 shows α_{solid} against x.

Hinuma *et al.*[13)] calculated entropy (S) of $LiFePO_4$ and $FePO_4$ by first principles calculation. Figure 4.5 shows the calculated S of $LiFePO_4$ and $FePO_4$ per formula unit. In both materials, S monotonously increases with temperature. $\Delta S_{\mathrm{solid}}$ ($= S_{\mathrm{LiFePO_4}} - S_{\mathrm{FePO_4}}$, where $S_{\mathrm{LiFePO_4}}$ and $S_{\mathrm{FePO_4}}$ are S of $LiFePO_4$ and $FePO_4$, respectively) increases with temperature and reaches at 0.30 meV/K at 300 K. Thus, the calculated $\Delta S_{\mathrm{solid}}$ explains the residual amount (= 0.44 mV/K) of α.

Chapter 5

*P*2-Na_xCoO_2

5.1 Introduction

Among materials for sodium ion secondary batteries, Na_xCoO_2 with $P2$-type structure ($P6_3/mmc$, $Z = 2$) is most intensively investigated.[16,30–34] In the $P2$-type structure, the edge-sharing CoO_2 layer and Na sheet are alternately stacked (Fig. 5.1). The close-packed oxygen sheets stack as AB|BA, in a sharp contrast to the AB|CA|BC stacking in the α-$NaFeO_2$ structure. As a result, the Na site is surrounded by the oxygen triangular prism. The compound shows a discharge capacity of 130 mAh/g and an average operating voltage of $\sim$ 2.5 V against Na in the sodium-ion secondary battery (SIB). From the point of view other than electrochemical properties, Na_xCoO_2 was intensively investigated due to its thermoelectoric properties,[35] superconductivity,[36] elecrtronic and magnetic properties.[37–39] Terasaki *et al.* reported lage thermoelectric power (= 0.1 mV/K at 300 K) in Na_xCoO_2 single crystal.[35] On the other hands, Tanaka *et al.* reported superconductivity at $T_C = 5$ K in $Na_xCoO_2 \cdot yH_2O$ ($x \sim 0.35, y \sim 1.3$).[38]

By means of first principles calculation, Hinuma *et al.*[16] have investigated the Na^+ ordering against the Na concentration (x). They found characteristic ordering of Na^+ at $x = 1/2$, 5/9, 3/5, 2/3, 5/7, 10/13, 13/16, 16/19, and 18/21. Consistently with the calculation, Berthelot *et al.*[32] reported a phase diagram of $P2$-Na_xCoO_2 and nine single-phases between $x = 0.5$ and 0.9 at room temperature. Among them, the $x = 1/2$ and 2/3 phases are intensively investigated and superstructures arising from sodium orderings are proposed.[40,41]

5.2 Results

Figure 5.2 shows the discharge curve (black curve) of $P2$-Na_xCoO_2 and its x-derivative (dV/dx; red curve). The overall behavior is consistent with the data reported by Delmas *et al.*[31] Discontinuous drops are observed at $x = 1/2$, 2/3, 0.74, 0.77, and 0.81 in the discharge curve. These concentrations are ascribed to the Na^+ ordered phases proposed by GGA first principles calculations.[16] The $x = 0.77$ and 0.81 drops can be ascribed to the 10/13- and 13/16- phases.[16] The $x = 0.74$ drop could be attributed to a metastable crossover point where the Na1 sites start to form triplets rather than being isolated. Chemically-synthesized $P2$-$Na_{0.5}CoO_2$ ($x = 1/2$)[42] and $P2$-$Na_{0.67}CoO_2$ ($x = 2/3$)[43] are reported to show superlattice reflections related to the Na^+ ordering.

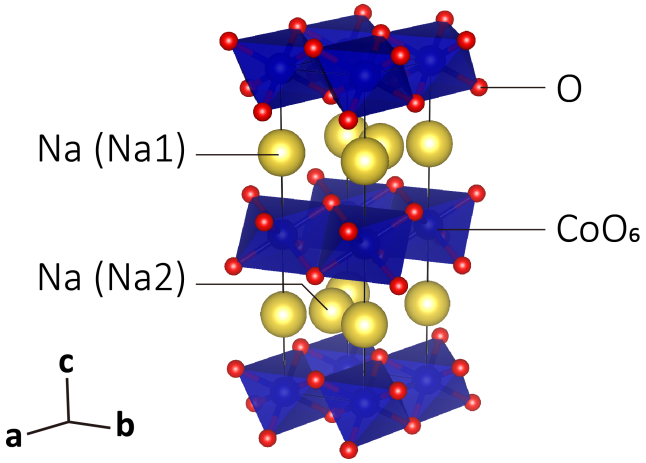

Figure 5.1: Crystal structure of $P2$-Na_xCoO_2. Large yellow spheres represent Na1 and Na2 sites. Blue octahedra and small red spheres represent Co and O, respectively.

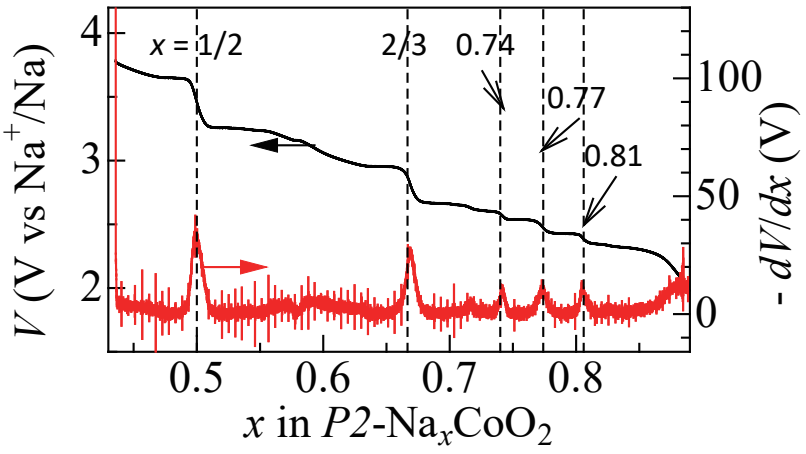

Figure 5.2: Discharge curve (black curve) of $P2$-Na_xCoO_2 and its x-derivative. The discharge curve was obtained at the first cycle. The data were cited and modified from Ref. [14)]

Figure 5.3 shows temperature dependence of V of $P2$-Na_xCoO_2: (a) $x = 0.51$, (b) 0.63, and (c) 0.72. Red closed and blue open symbols represent that the data were obtained in the heating and cooling runs, respectively. Both the data points are almost overlapped, indicating that the data are free from temperature gradient nor the sample deterioration. At (a) $x = 0.51$, V linearly increases with T. α (= 0.83 mV/K) was evaluated by least-squares fitting, as indicated by the broken straight line. At (b) $x = 0.63$, V is nearly independent of T. α (= 0.01 mV/K) was evaluated by least-squares fitting. At (c) $x = 0.72$, V linearly increases with T again. α (= 0.43 mV/K) was evaluated by least-squares fitting.

Figure 5.4 shows thus determined α of $P2$-Na_xCoO_2 against x. α scatters from 0.0 mV/K to 0.9 mV/K. For example, α steeply decreases from 0.83 mV/K at $x = 0.51$ to 0.01 mV/K at $x = 0.63$. Such a steep reduction of α in $P2$-Na_xCoO_2 makes sharp contrast with the nearly constant (= 0.91 mV/K) behavior of α in Li_xFePO_4 (Chapter 4).

Figure 5.5 shows solid component ($\alpha_{\rm solid} = \alpha - \alpha_{\rm electrolyte}$) of α of $P2$-Na_xCoO_2 against x. Here, let us evaluate temperature coefficient of redox potential ($\alpha^{\rm PS}_{\rm solid}$) within the framework of the phase separation (PS) model, which well explains $\alpha_{\rm solid}$ of Li_xFePO_4 as shown in Sec. 4.3. The discharge curve (Fig. 5.2) suggests formation of the single phases at $x = 1/2$, 2/3, 0.74, 0.77, and 0.81. Among then, the 1/2-, 2/3-, 0.77-, and 0.81-phases can be ascribed to the 1/2-, 2/3, 10/13-, and 13/16-phases proposed by first principles calculation.[16] Then, $\Delta S^{\rm PS}_{\rm solid}$ is simply expressed as

$$\Delta S^{\rm PS}_{\rm solid} = \frac{S\left(x_{i+1}\right) - S\left(x_i\right)}{x_{i+1} - x_i}, \tag{5.1}$$

where x_i is x of each single phase. Hinuma *et al.*[14] calculated entropy [$S(x)$] of $P2$-Na_xCoO_2 at $x = 1/2$, 2/3, 10/13, and 13/16 by first principles calculation. Figure 5.6 shows temperature dependence of calculated $S(x)$ per formula unit. $S(x)$ at 300 K are 0.6457, 0.6527, 0.6608, 0.6678 meV/K at $x = 1/2$, 2/3, 10/13, and 13/16, respectively. Solid line in Fig. 5.5 represents $\alpha^{\rm PS}_{\rm solid}$. The calculation cannot reproduce the x-dependence of $\alpha_{\rm solid}$ even qualitatively, especially, the steep reductions in $\alpha_{\rm solid}$ from $x = 0.51$ to 0.63 and from $x = 0.68$ to 0.74. We note that this unexpected disagreement should be ascribed to the PS model itself, because the steep reduction cannot be reproduced even if another set of $S(x_i)$ is used.

5.3 Discussion

What is the origin of the unexpected disagreement between experientially-obtained $\alpha_{\rm solid}$ and $\alpha^{\rm PS}_{\rm solid}$? We think that the answer is in the phase boundary between the two Na^+ ordered phases. Figure 5.7(a) schematically shows the phase boundary between 0- and 1-phases. Such a phase boundary actually exists in Li_xFePO_4.[20] In this case, Li^+ intercalation takes place at the interface area.[17,20] Important point is that the Li^+ intercalation at the interface area moves the phase boundary to the left side. We call such a boundary as "mobile" boundary. The situation is completely different in the phase boundary between 1/2- and 2/3-phases, as schematically shown in Fig. 5.7(b). Similar to the case of "mobile" boundary, Na^+ intercalation is considered to take place at the interface area. The Na^+ intercalation, however, cannot move the phase boundary, because addition of Na^+ on the 1/2-phase cannot produce the 2/3-type ordering. We call such a boundary as "immobile" boundary.

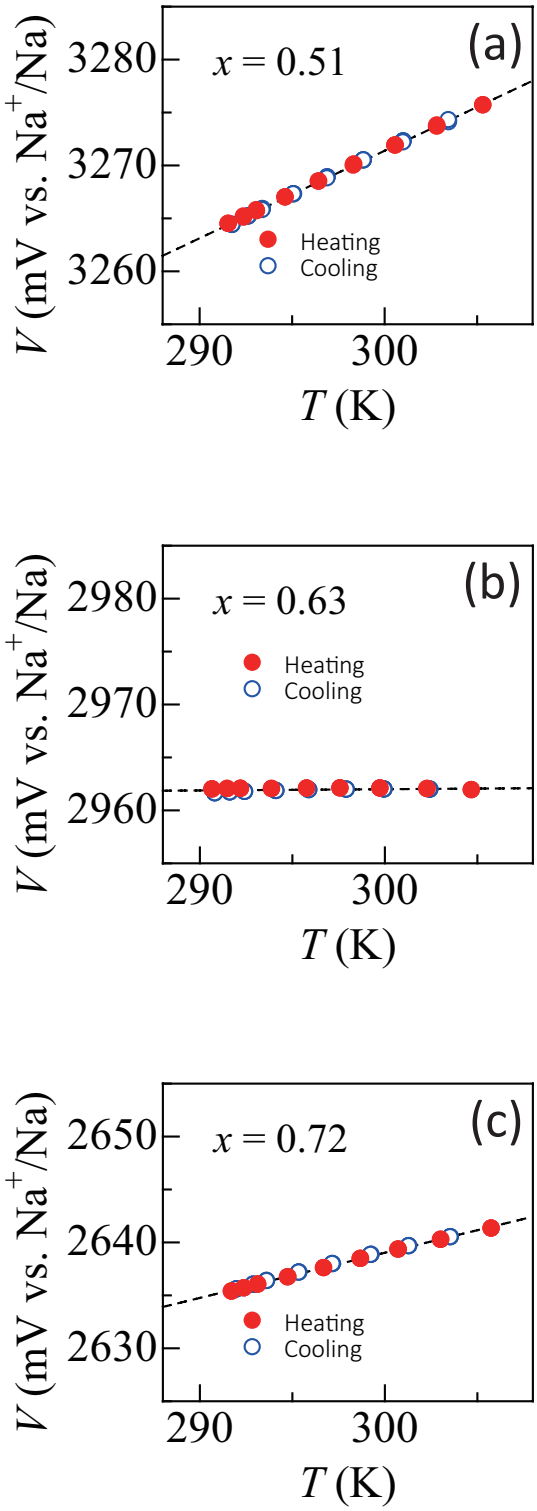

Figure 5.3: Temperature dependence of V of Na_xCoO_2: (a) $x = 0.51$, (b) 0.63, and (c) 0.72. Red closed and blue open symbols represent that the data were obtained in the heating and cooling runs, respectively. Straight lines are results of least-squares fittings. The data were cited and modified from Ref. [14)]

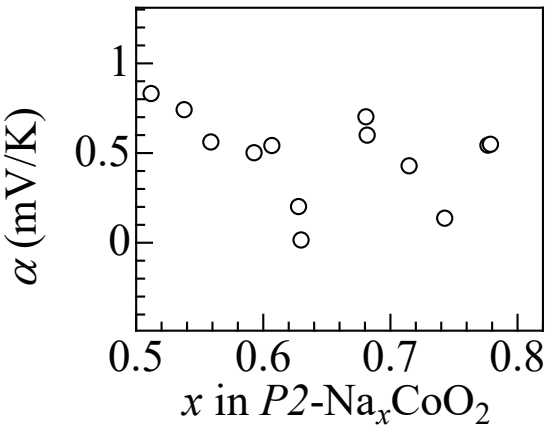

Figure 5.4: Temperature coefficient (α) of redox potential of $P2$-Na_xCoO_2 against x. The data were cited and modified from Ref. [14)]

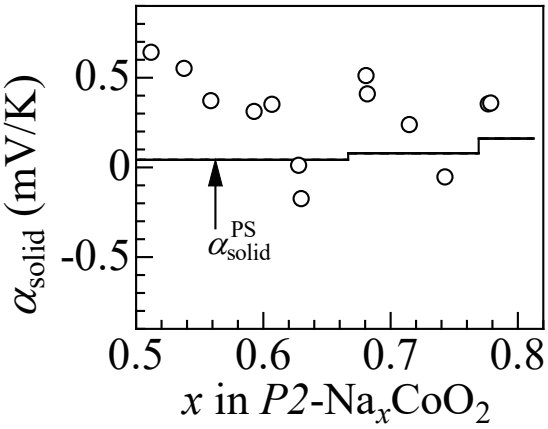

Figure 5.5: Solid component ($\alpha_{\rm solid} = \alpha - \alpha_{\rm electrolyte}$) of α of $P2$-Na_xCoO_2 against x. The solid line represents calculated $\alpha^{\rm PS}_{\rm solid}$. The data were cited and modified from Ref. [14)]

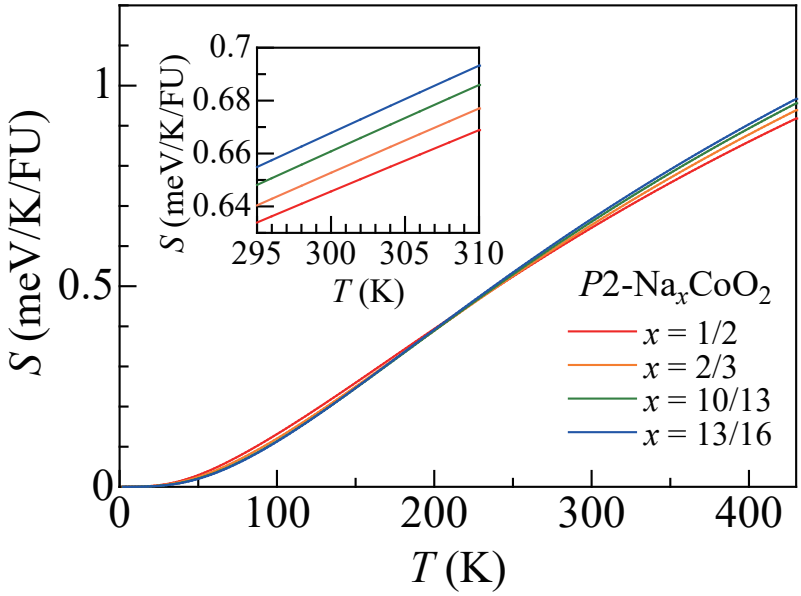

Figure 5.6: Temperature dependence of calculated entropy (S) for Na_xCoO_2 at $x = 1/2$, 2/3, 10/13, and 13/16. The inset shows magnified data. The data were cited and modified from Ref. [14)]

Nevertheless, the Na^+ intercalation and consequent phase transformation takes place in the actual $P2$-Na_xCoO_2 system. Most probable scenario for the phase transformation is formation of the pseudo-disordered region between the 1/2- and 2/3-phases, in which the Na^+ ordering gradually changes from the 1/2- to 2/3-types. In such a pseudo-disordered region, the Na^+ migration is possible to move the phase boundary to the left side.

Here, let us phenomenologically include the effect of the configuration entropy ($S^{\rm cf}_{\rm solid}$) in the pseudo-disordered region. Exact treatment of such a region, however, is difficult due to the residual correlation between Na^+. So, we crudely approximate $S^{\rm cf}_{\rm solid}$ in the disorder limit as

$$S^{\rm cf}_{\rm solid} = k_{\rm B}\ln\frac{(x_{i+1}-x_i)!}{(x_{\rm dis}-x_i)!\,(x_{i+1}-x_{\rm dis})!}. \tag{5.2}$$

where $x_{\rm dis}$ is the Na concentration in the pseudo-disordered region. Generally speaking, $x_{\rm dis}$ is different from the entire x except at x_i, where the system becomes simple phase. Here, we approximate $x_{\rm dis}$ to the entire x. Then, the configuration component ($\alpha^{\rm cf}_{\rm solid}$) of α is given by

$$\alpha^{\rm cf}_{\rm solid} = \frac{1}{e}\frac{\partial S^{\rm cf}_{\rm solid}}{\partial x} = \frac{1}{e}k_{\rm B}\ln\frac{x_{i+1}-x}{x-x_i}. \tag{5.3}$$

The effective value ($\alpha^{\rm PS+cf}_{\rm solid}$) of α in the pseudo-disordered region is phenomenologically expressed as

$$\alpha^{\rm PS+cf}_{\rm solid} = (1-\beta)\,\alpha^{\rm PS}_{\rm solid} + \beta\alpha^{\rm cf}_{\rm solid}, \tag{5.4}$$

where β is a phenomenological parameter. Figure 5.8 shows the compression of $\alpha^{\rm PS+cf}_{\rm solid}$ and experimentally-obtained $\alpha_{\rm solid}$. The phenomenological model qualitatively reproduced the x-dependence of $\alpha_{\rm solid}$, including the steep reduction in $\alpha_{\rm solid}$ from $x = 0.51$ to 0.63 and from $x = 0.68$ to 0.74.

There still exists deviation between the phenomenological mode and experiment. Especially, the experimental data deviates to the positive side at $x = 0.51$–0.60 and 0.68–0.72. Such a deviation is

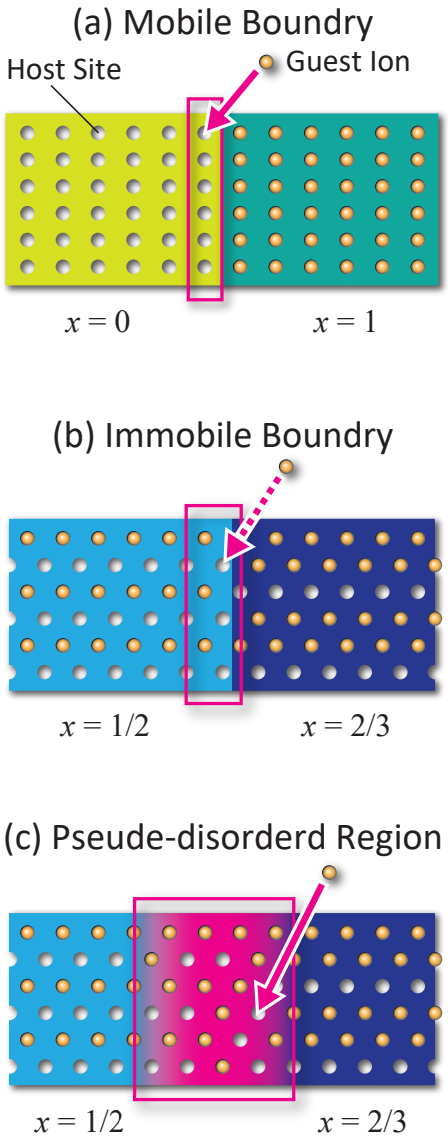

Figure 5.7: (a) Illustration of mobile phase boundary between the 0- and 1-phases, as exemplified by Li_xFePO_4. (b) Illustration of immobile phase boundary between the 1/2- and 2/3-phases, as exemplified by Na_xCoO_2. (c) Illustration of pseudo-disordered region between the 1/2- and 2/3-phases. The ordering patterns are simplified for inconvenience of explanation. The data were cited and modified from Ref. [14)]

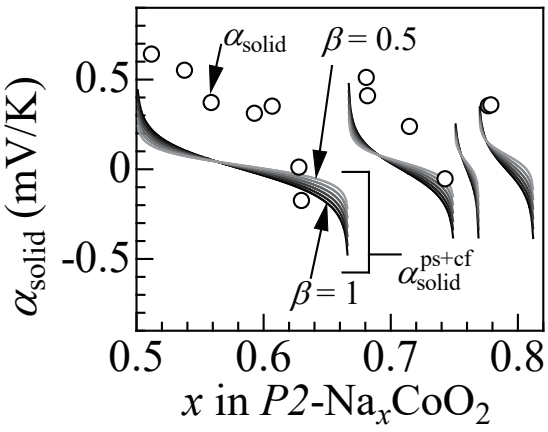

Figure 5.8: Solid component ($\alpha_{\rm solid} = \alpha - \alpha_{\rm electrolyte}$) of α of Na_xCoO_2 against x. Solid curve represents phenomenological model, $\alpha^{\rm PS+cf}_{\rm solid} = (1-\beta)\alpha^{\rm PS}_{\rm solid} + \beta\alpha^{\rm cf}_{\rm solid}$, where $\alpha^{\rm PS}_{\rm solid}$ and $\alpha^{\rm cf}_{\rm solid}$ are the phase separation and configuration components of α, respectively. The data were cited and modified from Ref. [14)]

probably ascribed to the too simplification of the model, that is, (1) the model completely neglects residual correlation between the Na sites and (2) $x_{\rm dis}$ is set to be x. We consider that the latter simplification causes the deviation. If the stability of the x_i- and x_{i+1}-phases are the same, $x_{\rm dis}$ is expected to be $(x_i + x_{i+1})/2$ except at $x = x_i$ and x_{i+1}. If the $x = 1/2$ phase is more stable than the $x = 2/3$ phase, which is expected in the actual $P2$-Na_xCoO_2 system, we expect $x_{\rm dis} \sim 1/2$ except at $x = 1/2$. Such a coordination transformation elongates the x-region where $\alpha^{\rm cf}_{\rm solid}$ shows high positive value ($\sim$ 0.5 mV/K; Fig. 5.9) and better explains the experimental observation. Similarly, if the $x = 2/3$ phase is more stable than the $x = 3/4$ phase, which is expected in the actual $P2$-Na_xCoO_2 system, we expect $x_{\rm dis} \sim 2/3$ except at $x = 3/4$.

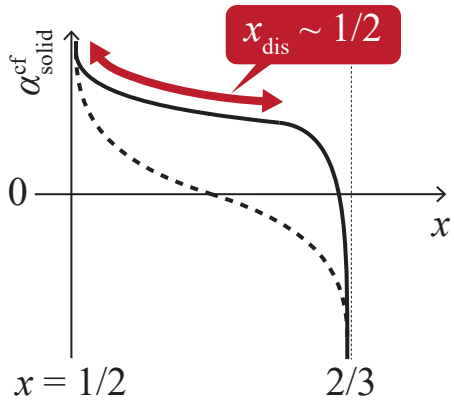

Figure 5.9: α^{cf}_{solid} against x. The broken curve represents a too-simplified case ($x_{dis} = x$). The solid curve represents a more realistic case.

Chapter 6

Prussian blue analogues

6.1 Introduction

Among the battery materials, PBAs, whose chemical formula are $\mathrm{Li}_x M[\mathrm{Fe(CN)_6}]_y$ and $\mathrm{Na}_x M[\mathrm{Fe(CN)_6}]_y$ (M is transition metal), are promising candidates for the cathode materials in lithium-ion/sodium-ion secondary batteries.[44–53] For example, thin film of $\mathrm{Li}_{1.60}\mathrm{Co}[\mathrm{Fe(CN)_6}]_{0.90}$ shows a high capacity of 132 mAh/g with a good cyclability.[46] Most of PBAs have the face-centered cubic (fcc) ($Fm\bar{3}m$; $Z = 4$) or trigonal ($R\bar{3}m$; $Z = 3$) structures.[54–56] They consist of three-dimensional (3D) jungle-gym-type host framework and guest $\mathrm{Li}^+/\mathrm{Na}^+$ ions and $\mathrm{H_2O}$ molecules, which are accommodated in nanopores of the framework (Fig. 6.1). The framework contains considerable $[\mathrm{Fe(CN)_6}]$ vacancies (10%–30%). The discharge curves of Co- and Mn-PBA show characteristic plateaus, whose redox reactions were well assigned by means of X-ray absorption spectroscopy.[21–23,45,57] Recently, the α values were reported in $\mathrm{Li}_x\mathrm{Co}[\mathrm{Fe(CN)_6}]_{0.71}$ and $\mathrm{Li}_x\mathrm{Co}[\mathrm{Fe(CN)_6}]_{0.90}$ against x.[58] In this report, however, the cathode and anode temperatures were the same as the temperature (T_{cell}) of the thermocell. Thus evaluated α corresponds to the difference between those of cathode (PBA) and anode (Li) materials.

6.2 Results

Figure 6.2 shows discharge curves of (a) $\mathrm{Na}_x\mathrm{Co}[\mathrm{Fe(CN)_6}]_{0.71}$ (NCF71), (b) $\mathrm{Na}_x\mathrm{Co}[\mathrm{Fe(CN)_6}]_{0.90}$ (NCF90) and (c) $\mathrm{Na}_x\mathrm{Mn}[\mathrm{Fe(CN)_6}]_{0.83}$ (NMF83) films. The curve of NCF71 [(a)] shows a single plateau around 3.4 V, which is ascribed to the reduction reaction:[21–23]

$$\mathrm{Na}_{0.13}\mathrm{Co}^{\mathrm{II}}[\mathrm{Fe}^{\mathrm{III}}(\mathrm{CN})_6]_{0.71} + 0.71\,\mathrm{Na}^+ + 0.71e^- \longrightarrow \mathrm{Na}_{0.84}\mathrm{Co}^{\mathrm{II}}[\mathrm{Fe}^{\mathrm{II}}(\mathrm{CN})_6]_{0.71}. \tag{6.1}$$

In the discharge process, Na^+ ions are inserted into the framework, which causes the reduction of Fe^{3+} to keep the charge neutrality. For convenience of explanation, we call this plateau "Plateau I." The curve of NCF90 [(b)] shows two plateaus around 3.8 and 3.2 V. The plateau around 3.8 V is ascribed to the reaction:[58]

$$\mathrm{Co}^{\mathrm{III}}[\mathrm{Fe}^{\mathrm{III}}(\mathrm{CN})_6]_{0.60}[\mathrm{Fe}^{\mathrm{II}}(\mathrm{CN})_6]_{0.30} + 0.60\,\mathrm{Na}^+ + 0.60e^- \longrightarrow \mathrm{Na}_{0.60}\mathrm{Co}^{\mathrm{III}}[\mathrm{Fe}^{\mathrm{II}}(\mathrm{CN})_6]_{0.90}. \tag{6.2}$$

The plateau around 3.2 V is ascribed to the reaction:

$$\mathrm{Na}_{0.60}\mathrm{Co}^{\mathrm{III}}[\mathrm{Fe}^{\mathrm{II}}(\mathrm{CN})_6]_{0.90} + \mathrm{Na}^+ + e^- \longrightarrow \mathrm{Na}_{1.60}\mathrm{Co}^{\mathrm{II}}[\mathrm{Fe}^{\mathrm{II}}(\mathrm{CN})_6]_{0.90}. \tag{6.3}$$

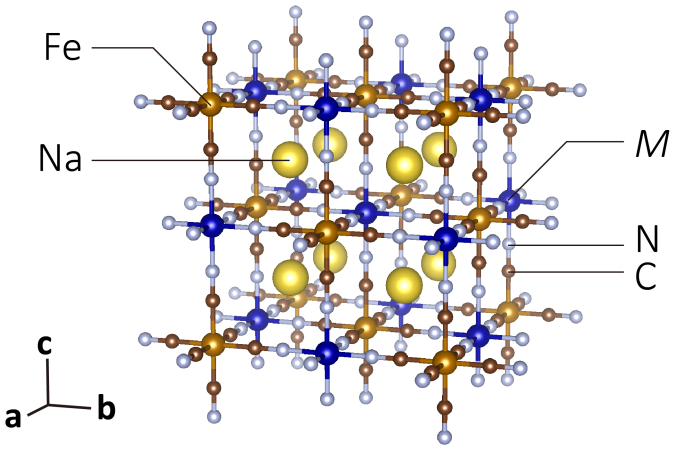

Figure 6.1: Crystal structure of Prussian blue analog ($Na_xM[Fe(CN)_6]_y$). M represents transition metal. For simplicity, H_2O is omitted.

For convenience of explanation, we call the plateaus around 3.8 V and 3.2 V "Plateau II" and "Plateau III," respectively. The redox potential (V) for Fe^{3+}/Fe^{2+} in NCF90 ($\sim$ 3.8 V; Plateau II) is much higher than that in NCF71 ($\sim$ 3.4 V; Plateau I). The high-V is ascribed to the volume effect. Actually, the lattice constant ($a \sim 9.9$ Å at $x < 0.6$)[58] of NCF90 is much smaller than a (10.2–10.3 Å)[21–23] of NCF71. The curve of NMF83 [(c)] shows two plateaus around 3.7 and 3.3 V. The plateau around 3.7 V is ascribed to the reaction:[58]

$$Mn^{III}_{0.49}Mn^{II}_{0.51}[Fe^{III}(CN)_6]_{0.83} + 0.49\,Na^+ + 0.49e^- \longrightarrow Na_{0.49}Mn^{II}[Fe^{III}(CN)_6]_{0.83}. \quad (6.4)$$

The plateau around 3.3 V is ascribed to the reaction:

$$Na_{0.49}Mn^{II}[Fe^{III}(CN)_6]_{0.83} + 0.83\,Na^+ + 0.83e^- \longrightarrow Na_{1.32}Mn^{II}[Fe^{II}(CN)_6]_{0.83}. \quad (6.5)$$

For convenience of explanation, we call the plateaus around 3.7 V and 3.3 V "plateau IV" and "plateau V," respectively. The redox potential (V) for Fe^{3+}/Fe^{2+} in NMF83 ($\sim$ 3.3 V; Plateau V) is comparable to that in NCF71 ($\sim$ 3.4 V; Plateau I), because a ($\sim$ 10.9 Å at $x < 0.49$)[21–23] of NMF83 is large enough.

Figure 6.3 shows temperature dependence of V in the respective plateaus. Blue open and red closed symbols represent the data obtained in the cooling and heating runs, respectively. α in the respective runs was evaluated by least-squares fitting, as indicated by solid straight line. Note that the temperature effect on V in the anode (Na metal) is negligible, because T_{anode} is fixed at 295 K during the measurements. In the lower-lying plateaus, *i.e.*, Plateau I [(a)], III [(c)], and V [(e)], the data obtained in the cooling and heating runs are almost overlapped. Interestingly, α is found to be negative in Plateau V [(e)]. In the higher-lying plateaus, *i.e.*, Plateau II [(b)] and IV [(d)], however, deviations are discernible between the cooling and heating runs. We tentatively defined the average between the cooling and heating runs as α. Figure 6.4 shows thus determined α against x in (a) NCF71, (b) NCF90, and (c) NMF83. In NCF71 [(a)], α distributes around 0.6 mV/K except for the high x-region ($x > 0.8$) near the edge of the discharge curve. In NCF90 [(b)], α distributes around

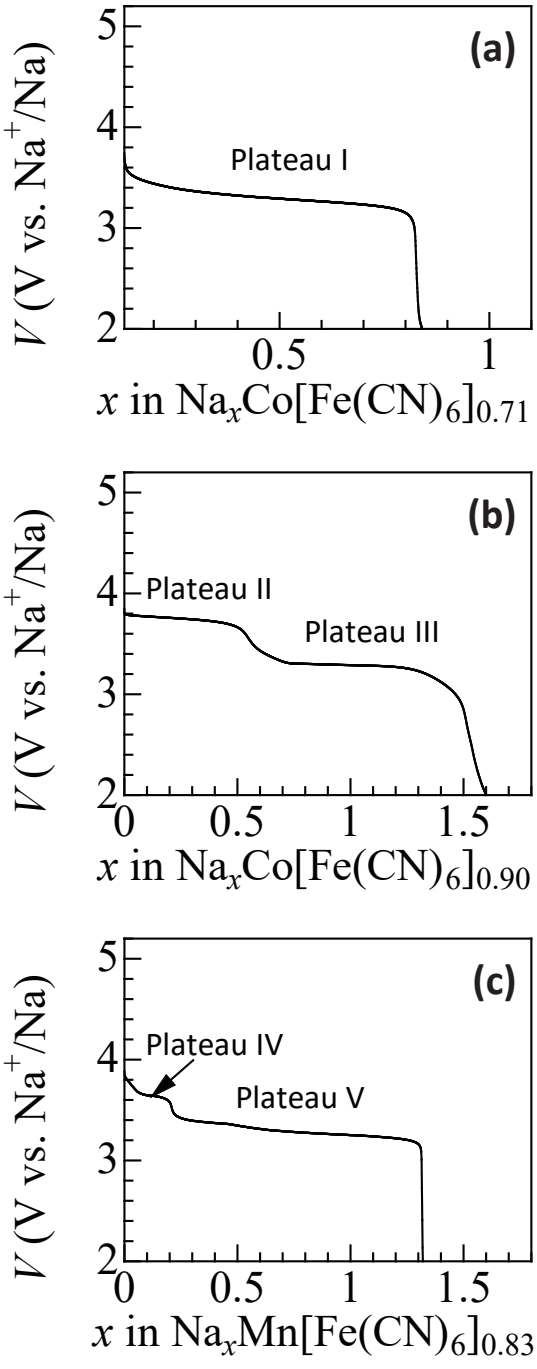

Figure 6.2: Discharge curves of (a) $Na_xCo[Fe(CN)_6]_{0.71}$ (NCF71), (b) $Na_xCo[Fe(CN)_6]_{0.90}$ (NCF90) and (c) $Na_xMn[Fe(CN)_6]_{0.83}$ (NCF83) discharged at 0.1 C. For convenience of explanation, we defined Plateaus I, II, II, IV, and V. The data were cited and modified from Ref. [59)]

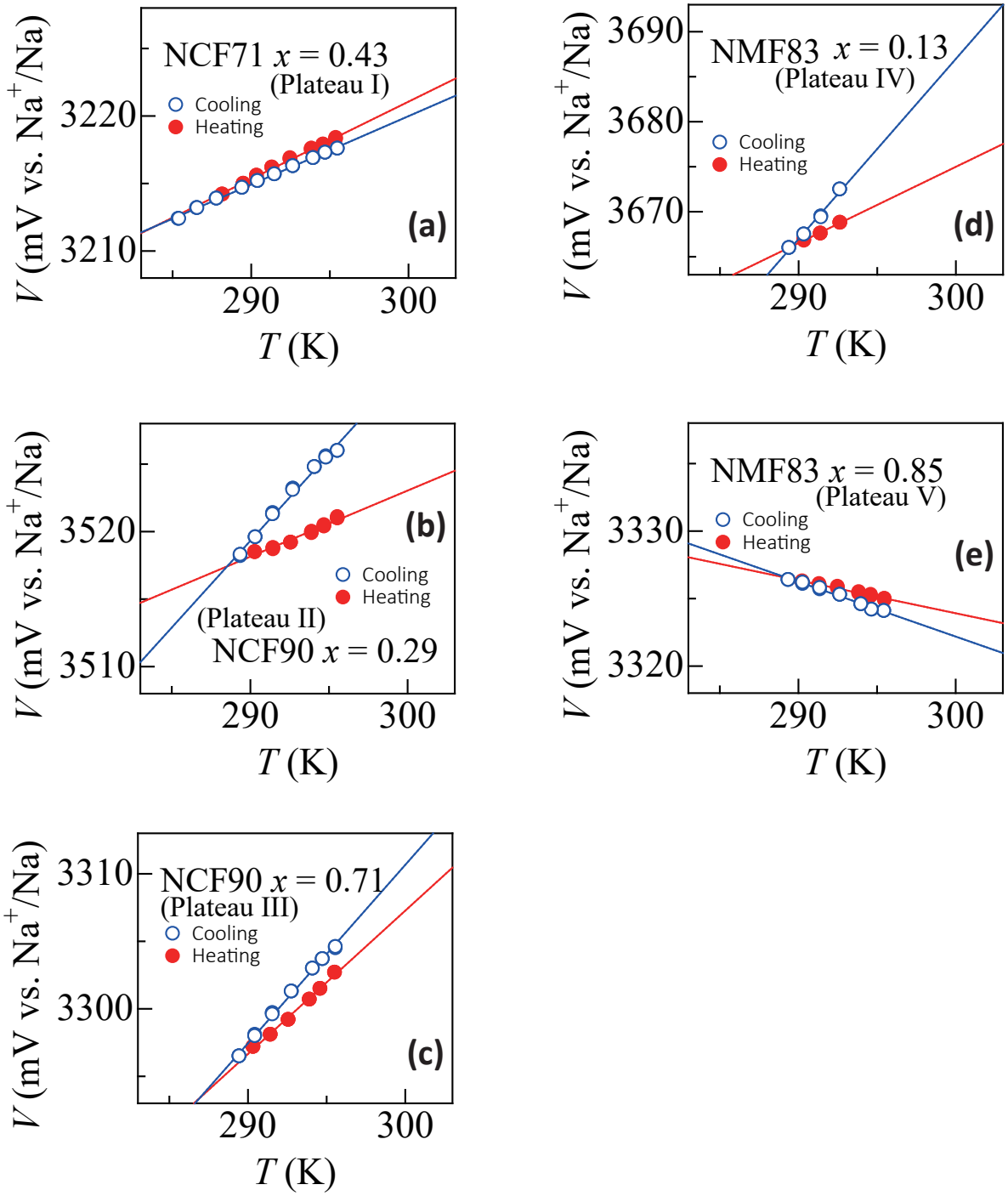

Figure 6.3: Temperature dependence of V in respective plateaus: (a) Plateau I, (b) Plateau II, (c) Plateau III, (d) Plateau IV, and (e) Plateau V. Temperature (T_{anode}) of anode is fixed at 295 K. Blue open and red closed symbols represent the data obtained in the cooling and heating runs, respectively. Solid straight lines are results of the least-squares fitting. I–V represent the respective plateaus. The data were cited and modified from Ref. [59)]

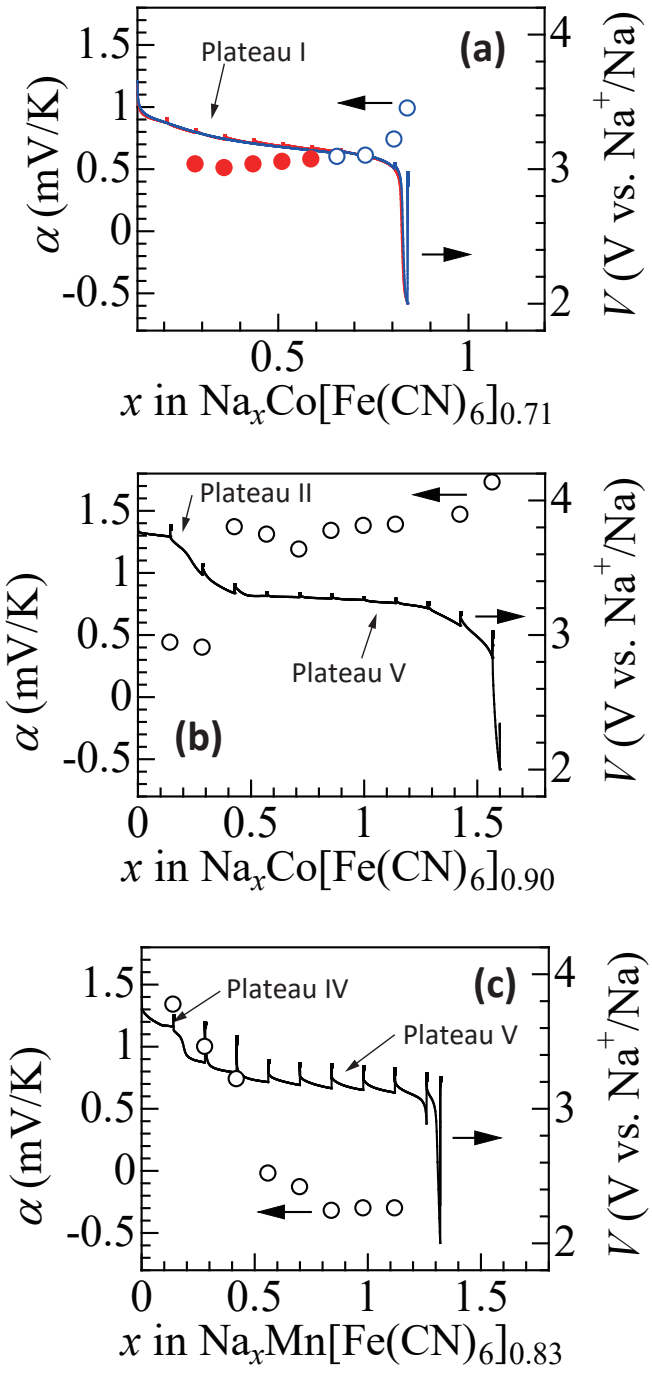

Figure 6.4: Temperature coefficient (α) of redox potential of (a) NCF71, (b) NCF90 and (c) NCF83 against x. Discharge curves at the respective measurements are also plotted. The red and blue symbols in (a) represent the data obtained at the second and third discharge runs, respectively. The data were cited and modified from Ref. [59)]

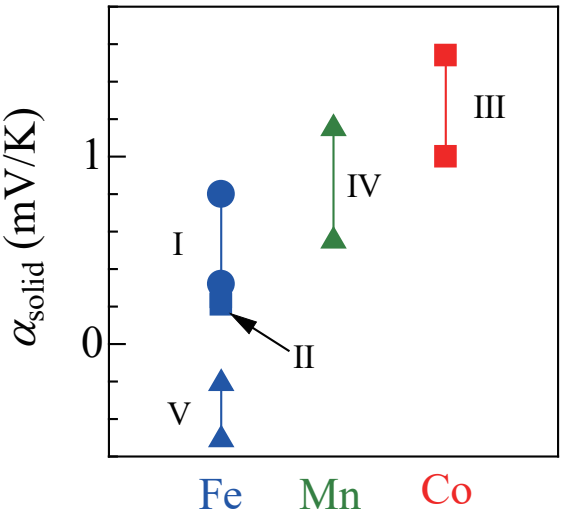

Figure 6.5: Redox cite dependence of α_{solid}. I–V represent the respective plateaus. Vertical lines represent the distribution of α_{solid} at each plateaus.

0.4 mV/K and 1.4 mV/K in Plateau II and III, respectively. In NMF83 [(c)], α shows rather gradual decrease with x from 1.4 mV/K at $x = 0.15$ to -0.2 mV/K at $x = 0.72$. Especially, α distributes around -0.4 mV/K in the region of $x > 0.8$. The magnitude and sign of α significantly depend not only on the material but also the redox site.

6.3 Discussion

The investigated PBAs do not show phase separation. Then, we should consider the variation of entropy when one electron and one Na^+ are added.

First, let us consider the effect of the electron addition on $\Delta S_{\mathrm{solid}}$. The electron addition to PBA changes the valence state of the transition metal (M) from trivalent to divalent states. Such a valence change should change the $3d$-electron configuration including the spin state. Figure 6.5 shows redox cite dependence of α_{solid}. I–V represent the respective plateaus. We found that α_{solid} is the highest ($\sim$ 1.3 mV/K) for the Co redox and is the lowest (-0.4–0.6 mV/K) for the Fe redox, even though there exists rather larger distribution of the data point (vertical lines in Fig. 6.5). So, we first compare the interrelation between the variation (ΔS_{3d}) of the $3d$-electron configuration entropy and the experiment.

The contribution of the $3d$-electron configuration entropy (S_{3d})[60] on α is expressed as

$$\frac{1}{e}\Delta S_{3d} = \frac{1}{e}\left(S_{3d}^{\mathrm{di}} - S_{3d}^{\mathrm{tri}}\right), \tag{6.6}$$

where S_{3d}^{di} and S_{3d}^{tri} are the configuration entropy in the divalent and trivalent states, respectively. S_{3d} is expressed as

$$S_{3d} = k_{\mathrm{B}} \ln W \tag{6.7}$$

$$= k_{\mathrm{B}} \ln \left(N_{\mathrm{spin}} \times N_{\mathrm{orbital}}\right), \tag{6.8}$$

Table 6.1: $3d$-electron configuration entropy (S_{3d}).

Ion	Electronic configuration	S_{3d}	$\alpha_{\rm cal}$ ($= \frac{1}{e}\Delta S_{3d}$)
Co^{2+}	$e_g^2 t_{2g}^5$	$k_{\rm B}\ln(4\times 3)$	0.21 mV/K
Co^{3+}	$e_g^0 t_{2g}^6$	$k_{\rm B}\ln(1\times 1)$	
Mn^{2+}	$e_g^2 t_{2g}^3$	$k_{\rm B}\ln(6\times 1)$	-0.04 mV/K
Mn^{3+}	$e_g^1 t_{2g}^3$	$k_{\rm B}\ln(5\times 2)$	
Fe^{2+}	$e_g^0 t_{2g}^6$	$k_{\rm B}\ln(1\times 1)$	-0.15 mV/K
Fe^{3+}	$e_g^0 t_{2g}^5$	$k_{\rm B}\ln(2\times 3)$	

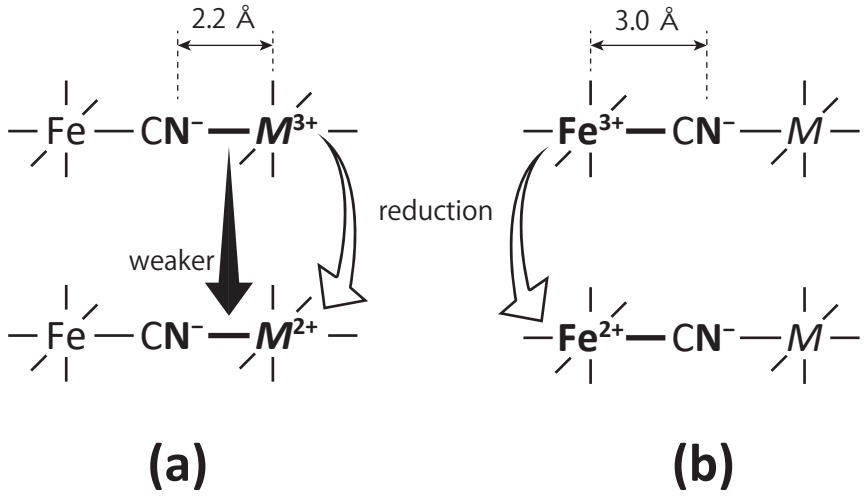

Figure 6.6: Schematic illustration of cyano-bridged transition metal network of Prussian blue analogues in (a) M ($=$ Co, Mn) reduction and (b) Fe reduction. Fe–N and M–N distances in NMF83 at 340 K[54,55] are also shown as an example.

where W, $N_{\rm spin}$, and $N_{\rm orbital}$ are the number of degenerate electronic configuration, spin degrees of freedom, and orbital degrees of freedom, respectively. $S_{3d}^{\rm di}$ and $S_{3d}^{\rm tri}$ of Co, Mn, Fe, and the numerical evaluation of $\alpha_{\rm cal}$ ($= \frac{1}{e}\Delta S_{3d}$) are summarized in Table 6.1. $N_{\rm spin}$ is expressed as $2S+1$, where S is the total spin quantum number. In PBAs, the oxidation process of Co^{2+} causes spin state transition from high-spin (Co^{2+}) to low-spin (Co^{3+}) states. The redox process of Co^{2+}/Co^{3+} contributes to α by 0.21 mV/K while that of Fe^{2+}/Fe^{3+} contributes to α by -0.15 mV/K. This argument is qualitatively consistent with the experimental observation that $\alpha_{\rm solid}$ is the highest (~ 1.3 mV/K) for the Co redox and is the lowest (-0.4–0.6 mV/K) for the Fe redox, even though there still exist discrepancy between the experiment and the ΔS_{3d}.

One possible origin for the discrepancy may be variation ($\Delta S_{\rm vi}$) of the vibrational entropy of the CN^- related mode, *e.g.*, stretching and vending mode of CN^-, induced by the valence change of the neighboring transition metal sites (Fig. 6.6). We emphasize that carbon atom of CN^- links to Fe while nitrogen atom links to M in the cyano-bridged transition metal network. Then, $\Delta S_{\rm vi}$ is expected to show redox site dependence between Fe and M. When M is reduced from trivalent to

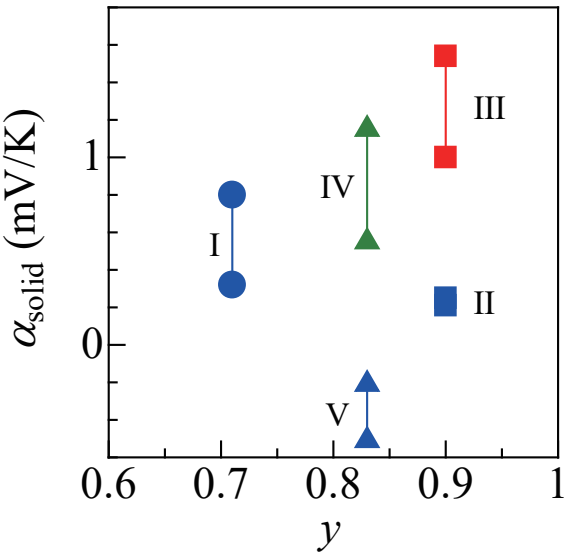

Figure 6.7: $[Fe(CN)_6]$ concentration (y) dependence of α_{solid}. I–V represent the respective plateaus. Vertical lines represent the distribution of α_{solid} at each plateaus.

divalent state, the electrostatic force between $M^{3+/2+}$ and N^- becomes weaker [Fig. 6.6 (a)]. Then, the frequency of the CN^- related mode decreases and vibrational entropy increases. Then, $\Delta S_{\mathrm{solid}}$ due to vibrational entropy is positive. The corresponding effect is considered to be suppressed when Fe is reduced, because Fe–N distance (*e.g.* $\sim$ 3.0 Å for NMF83[54,55]) is much longer than the M–N distance (*e.g.* $\sim$ 2.2 Å for NMF83[54,55]) [Fig. 6.6 (b)]. This argument is qualitatively consistent with the experimental observation that α_{solid} for Co/Mn redox is higher than that for the Fe redox (Fig. 6.5).

By contrast, PBA has significant amount of $[Fe(CN)_6]$ deficiencies $(1-y)$. There exists a rather large space around the $[Fe(CN)_6]$ deficient site. Then, Na^+ may approach to the CN^- ligand to reduce the electrostatic energy. Such a local structure may affect the entropy. We, however, found no clear correlation between y and α_{solid}, as shown in Fig. 6.7.

Chapter 7

Summary

We systematically investigated the solid component (α_{solid}) of α in three prototypical cathode materials for Li- and Na-ion secondary batteries, thai is, $\mathrm{Li}_x\mathrm{FePO}_4$, $P2$-$\mathrm{Na}_x\mathrm{CoO}_2$, and Prussian blue analogues.

$\mathrm{Li}_x\mathrm{FePO}_4$ shows ideal phase separation into FePO_4 and LiFePO_4, as $\mathrm{Li}_x\mathrm{FePO}_4 \longrightarrow (1-x)\mathrm{FePO}_4$ and $x\mathrm{LiFePO}_4$. As expected, α_{solid} is well reproduced by $\frac{1}{e}\left(S_{\mathrm{LiFePO}_4} - S_{\mathrm{FePO}_4}\right)$.

$P2$-$\mathrm{Na}_x\mathrm{CoO}_2$ shows successive phase transition at specific Na concentration (x_i; $i = 1, 2, 3, \dots$) accompanying ordering of Na^+ ions, and hence, phase separation is expected at the intermediation Na concentration (x; $x_i < x < x_{i+1}$). However, the phase separation model fails to reproduce the characteristic x-dependence of α_{solid}. We discussed this unexpected with introducing a pseud-disordered region around the phase boundary. In such a region, the configuration entropy of Na^+ ion plays a significant role, which partially improve the discrepancy between the experiment and the phase separation mode.

The three Prussian blue analogues do not show phase separation. Then, we should consider the effect on $\Delta S_{\mathrm{solid}}$, when one Na^+ and one electron are added to the Prussian blue analogues. We observed characteristic redox site dependence of α_{solid}: α_{solid} is the highest for the Co redox and the lowest for the Fe redox. The behavior is interpreted in term of (1) configuration entropy of the $3d$-electrons and (2) vibrational entropy of the CN^- related vibration.

Acknowledgments

This work was supported by Grant-in-Aid for JSPS Fellows (19J12284) from the Japan Society for the Promotion of Science. The synchrotron-radiation X-ray powder diffraction experiments were performed at the SPring-8 BL02B2 beamline with the approval of the Japan Synchrotron Radiation Research Institute (JASRI). Design and fabrication of the thermocell was supported by Engineering Workshop Division, Research Facility Center for Science and Technology, University of Tsukuba.

I would like to express my gratitude to all the professors and students and persons who supported this study.

Professor Yutaka Moritomo spent enormous efforts for leading this study and gave me critical comments from not only the physics view point but also the point of view of a scientist. I am so grateful to Professor Yutaka Moritomo as not to be able to express my gratitude. Professor Eiji Nishibori, Professor Akinobu Kanda, and Associate Professor Masashige Onoda gave me helpful suggestions and critical readings of the manuscript. I express a deep sense of gratitude.

Assistant Professor (Lecturer) Kazuyuki Higashiyama, Assistant Professor Wataru Kobayashi, Assistant Professor Hideharu Niwa, and Associate Professor Takayuki Shibata (National Institute of Technology, Gunma College) gave me grateful advice and experimental support. Dr. Yoyo Hinuma (Tokyo Institute of Technology) gave me grateful advice from the point of view of computational science. Professor Sankei Hori (Engineering Workshop Division) and Mr. Shoji Yoshizumi (Engineering Workshop Division) processed many parts of the thermocell with clockwork precision despite extremely difficult demands. Dr. Ichiro Nagai, Dr. Yasuyo Ogino (Kanagawa University), Mrs. Kyoko Kimura, Mr. Kohei Yonezawa, Mr. Kaoru Amaha, Mr. Shinji Iouno, Mr. Mitsuhiko Nakada, Mr. Shoma Higuchi, Mr. Yoshihiko Okazaki, Mr. Tetsu Ito, Mr. Yusuke Fujiwara, Mr. Toshiaki Moriya, Mr. Hiroki Iwaizumi, Mr. Tomotsugu Sugano, Mr. Hiroki Tachihara, Mr. Dai Inoue, Mr. Arnold Hendharto Widdhiarta, Mr. Yosuke Shimaura, Mr. Li Si Qi, Mr. Xue Qinglong, Mr. Taito Inoue, Mr. Toshiki Komatsu, Mr. Masato Sarukura, and Mr. Yuma Yoshida supported me in various points at the university. Dr. Masamitsu Takachi, Mr. Shota Urase, Mr. Ayumu Yanagita, Mr. Shota Akama, Ms. Akemi Kinoshita, and Mr. Rögnvaldur Líndal Magnússon encouraged me in my student life in my private time. I would like to express my thanks.

Finally, I am grateful to my family for their support and encouragement in every way through my long student life. Thank you very much indeed.

Bibliography

[1] J de Jong. Favourable results with the application of electrically driven heat pumps. II. PNEM heat pump in district heating with industrial waste heat as source of heat. *Elektrotechniek*, 68(1):30–35, 1990.

[2] Augustine N Ajah, Anish C Patil, Paulien M Herder, and Johan Grievink. Integrated conceptual design of a robust and reliable waste-heat district heating system. *Applied thermal engineering*, 27(7):1158–1164, 2007.

[3] Inger-Lise Svensson, Johanna Jönsson, Thore Berntsson, and Bahram Moshfegh. Excess heat from kraft pulp mills: Trade-offs between internal and external use in the case of Sweden-Part 1: Methodology. *Energy Policy*, 36(11):4178–4185, 2008.

[4] Vishal Garg. Building energy efficiency. 2009.

[5] Mamatha Dhananjaya and Manjunatha Reddy HS. A survey of energy harvesting sources for IoT device. *International Journal of Advanced Engineering, Management and Science*, 3(1), 2017.

[6] Maciej Haras and Thomas Skotnicki. Thermoelectricity for IoT–A review. *Nano Energy*, 54:461–476, 2018.

[7] Vladimir Leonov and Ruud JM Vullers. Wearable electronics self-powered by using human body heat: The state of the art and the perspective. *Journal of Renewable and Sustainable Energy*, 1(6):062701, 2009.

[8] Takayuki Shibata, Yuya Fukuzumi, Wataru Kobayashi, and Yutaka Moritomo. Thermal power generation during heat cycle near room temperature. *Appl. Phys. Express*, 11(1):017101, 2017.

[9] TI Quickenden and Y Mua. The power conversion efficiencies of a thermogalvanic cell operated in three different orientations. *Journal of The Electrochemical Society*, 142(11):3652–3659, 1995.

[10] Stefan Loos, Daniel Gruner, Mahmoud Abdel-Hafiez, Jürgen Seidel, Regina Hüttl, Anja UB Wolter, Klaus Bohmhammel, and Florian Mertens. Heat capacity (C_p) and entropy of olivine-type $LiFePO_4$ in the temperature range (2 to 773) K. *The Journal of Chemical Thermodynamics*, 85:77–85, 2015.

[11] Atsushi Togo, Laurent Chaput, Isao Tanaka, and Gilles Hug. First-principles phonon calculations of thermal expansion in Ti_3SiC_2, Ti_3AlC_2, and Ti_3GeC_2. *Phys. Rev. B*, 81(17):174301, 2010.

[12] Atsushi Togo and Isao Tanaka. First principles phonon calculations in materials science. *Scr. Mater.*, 108:1–5, 2015.

[13] Yuya Fukuzumi, Yoyo Hinuma, and Yutaka Moritomo. Temperature coefficient of redox potential of Li_xFePO_4. *AIP Adv.*, 8(6):065021, 2018.

[14] Yuya Fukuzumi, Yoyo Hinuma, and Yutaka Moritomo. Configuration Entropy Effect on Temperature Coefficient of Redox Potential of $P2$-Na_xCoO_2. *Jpn. J. Appl. Phys.*, 58(6):065501, 2019.

[15] Hiroki Iwaizumi, Tomotsugu Sugano, Takeshi Yasuda, Yukihiro Shimoi, Wataru Kobayashi, and Yutaka Moritomo. Vibrational entropy as an indicator of temperature coefficient of redox potential in conjugated polymers. *Japanese Journal of Applied Physics*, 58(9):097004, 2019.

[16] Yoyo Hinuma, Ying S Meng, and Gerbrand Ceder. Temperature-concentration phase diagram of $P2$-Na_xCoO_2 from first-principles calculations. *Phys. Rev. B*, 77(22):224111, 2008.

[17] Masamitsu Takachi and Yutaka Moritomo. In situ observation of macroscopic phase separation in cobalt hexacyanoferrate film. *Sci. Rep.*, 7:42694, 2017.

[18] E. Nishibori, M. Takata, K. Kato, M. Sakata, Y. Kubota, S. Aoyagi, Y. Kuroiwa, M. Yamakata, and N. Ikeda. The large Debye-Scherrer camera installed at SPring-8 BL02B2 for charge density studies. *Nuclear Instruments and Methods in Physics Research, Section A: Accelerators, Spectrometers, Detectors and Associated Equipment*, 467–468:1045–1048, 2001.

[19] Fujio Izumi and Koichi Momma. Three-dimensional visualization in powder diffraction. In *Solid State Phenomena*, volume 130, pages 15–20. Trans Tech Publ, 2007.

[20] C Delmas, M Maccario, L Croguennec, F Le Cras, and F Weill. Lithium deintercalation in $LiFePO_4$ nanoparticles via a domino-cascade model. *Nat. Mater.*, 7(8):665, 2008.

[21] F Nakada, H Kamioka, Y Moritomo, JE Kim, and M Takata. Electronic phase diagram of valence-controlled cyanide: $Na_{0.84-\delta}Co[Fe(CN)_6]_0.71 \cdot 3.8H_2O$ ($0 \leq \delta \leq 0.61$). *Physical review B*, 77(22):224436, 2008.

[22] K Igarashi, F Nakada, and Y Moritomo. Electronic structure of hole-doped Co-Fe cyanides: $Na_{1.60-\delta}Co[Fe(CN)_6]_{0.90} \cdot 2.9H_2O$ ($0.0 \leq \delta \leq 0.85$). *Physical review B*, 78(23):235106, 2008.

[23] Tomoyuki Matsuda, Masamitsu Takachi, and Yutaka Moritomo. A sodium manganese ferrocyanide thin film for Na-ion batteries. *Chemical Communications*, 49(27):2750–2752, 2013.

[24] Yuya Fukuzumi, Yoyo Hinuma, and Yutaka Moritomo. Thermal Coefficient of Redox Potential of Alkali Metals. *J. Phys. Soc. Japan*, 87(5):055001, 2018.

[25] Akshaya K Padhi, Kirakodu S Nanjundaswamy, and John B Goodenough. Phospho-olivines as positive-electrode materials for rechargeable lithium batteries. *Journal of the electrochemical society*, 144(4):1188–1194, 1997.

[26] Charles Delacourt, Philippe Poizot, Jean-Marie Tarascon, and Christian Masquelier. The existence of a temperature-driven solid solution in Li_xFePO_4 for $0 \leq x \leq 1$. *Nature materials*, 4(3):254, 2005.

[27] JL Dodd, Rachid Yazami, and Brent Fultz. Phase diagram of Li_xFePO_4. *Electrochemical and Solid-State Letters*, 9(3):A151–A155, 2006.

[28] Fei Zhou, Thomas Maxisch, and Gerbrand Ceder. Configurational electronic entropy and the phase diagram of mixed-valence oxides: the case of Li_xFePO_4. *Physical review letters*, 97(15):155704, 2006.

[29] Atsuo Yamada, Hiroshi Koizumi, Shin-ichi Nishimura, Noriyuki Sonoyama, Ryoji Kanno, Masao Yonemura, Tatsuya Nakamura, and Yo Kobayashi. Room-temperature miscibility gap in Li_xFePO_4. *Nature materials*, 5(5):357, 2006.

[30] C Fouassier, G Matejka, JM Reau, and P Hagenmuller. On new bronze oxides of formula Na_xCoO_2 ($x < 1$). System cobalt oxygen-sodium. *J. Solid State Chem*, 6:532, 1973.

[31] Claude Delmas, Jean-Jacques Braconnier, Claude Fouassier, and Paul Hagenmuller. Electrochemical intercalation of sodium in Na_xCoO_2 bronzes. *Solid State Ion.*, 3/4:165–169, 1981.

[32] Romain Berthelot, D Carlier, and Claude Delmas. Electrochemical investigation of the *P*2-Na_xCoO_2 phase diagram. *Nat. Mater.*, 10(1):74, 2011.

[33] M Medarde, M Mena, JL Gavilano, E Pomjakushina, J Sugiyama, K Kamazawa, V Yu Pomjakushin, D Sheptyakov, B Batlogg, HR Ott, et al. 1D to 2D Na^+ ion diffusion inherently linked to structural transitions in $Na_{0.7}CoO_2$. *Phys. Rev. Lett.*, 110(26):266401, 2013.

[34] Takayuki Shibata, Yuya Fukuzumi, Wataru Kobayashi, and Yutaka Moritomo. Fast discharge process of layered cobalt oxides due to high Na^+ diffusion. *Sci. Rep.*, 5:9006, 2015.

[35] Ichiro Terasaki, Yoshitaka Sasago, and Kunimitsu Uchinokura. Large thermoelectric power in $NaCo_2O_4$ single crystals. *Physical Review B*, 56(20):R12685, 1997.

[36] Kazunori Takada, Hiroya Sakurai, Eiji Takayama-Muromachi, Fujio Izumi, Ruben A Dilanian, and Takayoshi Sasaki. Superconductivity in two-dimensional CoO_2 layers. *Nature*, 422(6927):53, 2003.

[37] Michel Roger, DJP Morris, DA Tennant, MJ Gutmann, JP Goff, J-U Hoffmann, R Feyerherm, E Dudzik, D Prabhakaran, AT Boothroyd, et al. Patterning of sodium ions and the control of electrons in sodium cobaltate. *Nature*, 445(7128):631, 2007.

[38] Tomoaki Tanaka, Shin Nakamura, and Shuichi Iida. Observation of distinct metallic conductivity in $NaCo_2O_4$. *Japanese journal of applied physics*, 33(4B):L581, 1994.

[39] FC Chou, JH Cho, and YS Lee. Magnetic susceptibility study of hydrated and nonhydrated $Na_xCoO_2 \cdot yH_2O$ single crystals. *Physical Review B*, 70(14):144526, 2004.

[40] HW Zandbergen, M Foo, Q Xu, V Kumar, and RJ Cava. Sodium ion ordering in Na_xCoO_2: Electron diffraction study. *Physical Review B*, 70(2):024101, 2004.

[41] TA Platova, IR Mukhamedshin, H Alloul, AV Dooglav, and G Collin. Nuclear quadrupole resonance and x-ray investigation of the structure of $Na_{2/3}CoO_2$. *Physical Review B*, 80(22):224106, 2009.

[42] Maw Lin Foo, Yayu Wang, Satoshi Watauchi, H W Zandbergen, Tao He, R J Cava, and N P Ong. Charge Ordering, Commensurability, and Metallicity in the Phase Diagram of the Layered Na_xCoO_2. *Phys. Rev. Lett.*, 92(24):247001, 2004.

[43] T A Platova, I R Mukhamedshin, H Alloul, A V Dooglav, and G Collin. Nuclear quadrupole resonance and x-ray investigation of the structure of $Na_{2/3}CoO_2$. *Phys. Rev. B*, 80(22):224106, 2009.

[44] Tomoyuki Matsuda and Yutaka Moritomo. Thin film electrode of Prussian blue analogue for Li-ion battery. *Applied physics express*, 4(4):047101, 2011.

[45] Yutaka Moritomo, Masamitsu Takachi, Yutaro Kurihara, and Tomoyuki Matsuda. Thin film electrodes of Prussian blue analogues with rapid Li^+ intercalation. *Applied Physics Express*, 5(4):041801, 2012.

[46] Masamitsu Takachi, Tomoyuki Matsuda, and Yutaka Moritomo. Structural, electronic, and electrochemical properties of $Li_xCo[Fe(CN)_6]_{0.90}{\cdot}2.9H_2O$. *Japanese Journal of Applied Physics*, 52(4R):044301, 2013.

[47] Yuhao Lu, Long Wang, Jinguang Cheng, and John B Goodenough. Prussian blue: a new framework of electrode materials for sodium batteries. *Chemical communications*, 48(52):6544–6546, 2012.

[48] Masamitsu Takachi, Tomoyuki Matsuda, and Yutaka Moritomo. Cobalt hexacyanoferrate as cathode material for Na^+ secondary battery. *Applied Physics Express*, 6(2):025802, 2013.

[49] Dezhi Yang, Jing Xu, Xiao-Zhen Liao, Yu-Shi He, Haimei Liu, and Zi-Feng Ma. Structure optimization of Prussian blue analogue cathode materials for advanced sodium ion batteries. *Chemical Communications*, 50(87):13377–13380, 2014.

[50] Hyun-Wook Lee, Richard Y Wang, Mauro Pasta, Seok Woo Lee, Nian Liu, and Yi Cui. Manganese hexacyanomanganate open framework as a high-capacity positive electrode material for sodium-ion batteries. *Nature communications*, 5:5280, 2014.

[51] Long Wang, Jie Song, Ruimin Qiao, L Andrew Wray, Muhammed A Hossain, Yi-De Chuang, Wanli Yang, Yuhao Lu, David Evans, Jong-Jan Lee, et al. Rhombohedral Prussian white as cathode for rechargeable sodium-ion batteries. *Journal of the American Chemical Society*, 137(7):2548–2554, 2015.

[52] Shenglan Yu, Yong Li, Yunhao Lu, Ben Xu, Qiuting Wang, Mi Yan, and Yinzhu Jiang. A promising cathode material of sodium iron-nickel hexacyanoferrate for sodium ion batteries. *Journal of Power Sources*, 275:45–49, 2015.

[53] Ya You, Xing-Long Wu, Ya-Xia Yin, and Yu-Guo Guo. High-quality Prussian blue crystals as superior cathode materials for room-temperature sodium-ion batteries. *Energy & Environmental Science*, 7(5):1643–1647, 2014.

[54] Yutaka Moritomo, Tomoyuki Matsuda, Yutaro Kurihara, and Jungeun Kim. Erratum:"Cubic-Rhombohedral Structural Phase Transition in $Na_{1.32}Mn[Fe(CN)_6]_{0.83}\cdot 3.6H_2O$"[J. Phys. Soc. Jpn. 80, 074608 (2011)]. *Journal of the Physical Society of Japan*, 85(3), 2016.

[55] Yutaka Moritomo, Tomoyuki Matsuda, Yutaro Kurihara, and Jungeun Kim. Cubic-rhombohedral structural phase transition in $Na_{1.32}Mn[Fe(CN)_6]_{0.83}\cdot 3.6H_2O$. *Journal of the Physical Society of Japan*, 80(7):074608, 2011.

[56] Hideharu Niwa, Wataru Kobayashi, Takayuki Shibata, Hiroaki Nitani, and Yutaka Moritomo. Invariant nature of substituted element in metal-hexacyanoferrate. *Scientific reports*, 7(1):13225, 2017.

[57] Masamitsu Takachi, Tomoyuki Matsuda, and Yutaka Moritomo. Redox reactions in Prussian Blue analogue films with fast Na^+ intercalation. *Japanese Journal of Applied Physics*, 52(9R):090202, 2013.

[58] Rögnvaldur Líndal Magnússon, Wataru Kobayashi, Masamitsu Takachi, and Yutaka Moritomo. Temperature effect on redox voltage in $Li_xCo[Fe(CN)_6]_y$. *AIP advances*, 7(4):045002, 2017.

[59] Yuya Fukuzumi, Kaoru Amaha, Hideharu Niwa, Wataru Kobayashi, and Yutaka Moritomo. Prussian blue analogues as promising thermal power generation materials. *Energy Technol.*, 6(10):1865–1870, 2018.

[60] Hiroki Iwaizumi, Yusuke Fujiwara, Yuya Fukuzumi, and Yutaka Moritomo. The effect of 3D-electron configration entropy on the temperature coefficient of redoc potential in $Co_{1-z}Mn_z$ Prussian blue analogues. *Dalton trans.*, 48:1964–1968, 2019.

Related publications of this thesis

Chapter 3

Yuya Fukuzumi, Yoyo Hinuma, and Yutaka Moritomo. Thermal Coefficient of Redox Potential of Alkali Metals. *Journal of the Physical Society of Japan*, 87:055001, 2018.

Chapter 4

Yuya Fukuzumi, Yoyo Hinuma, and Yutaka Moritomo. Temperature coefficient of redox potential of Li_xFePO_4. *AIP Advances*, 8(6):065021, 2018.

Chapter 5

Yuya Fukuzumi, Yoyo Hinuma, and Yutaka Moritomo. Configuration Entropy Effect on Temperature Coefficient of Redox Potential of $P2$-Na_xCoO_2. *Japanese Journal of Applied Physics*, 58:065501, 2019.

Chapter 6

Yuya Fukuzumi, Kaoru Amaha, Wataru Kobayashi, Hideharu Niwa, and Yutaka Moritomo. Prussian Blue Analogues as Promising Thermal Power Generation Materials. *Energy Technology*, 6:1865, 2018.